Structure–Property–Function Relationships of Iron Oxide Multicore Nanoflowers in Magnetic Hyperthermia and Photothermia

Enzo Bertuit, Emilia Benassai, Guillaume Mériguet, Jean-Marc Greneche, Benoit Baptiste, Sophie Neveu, Claire Wilhelm, Ali Abou-Hassan

Enzo Bertuit, Emilia Benassai, Guillaume Mériguet, Jean-Marc Greneche, Benoit Baptiste, et al.. Structure–Property–Function Relationships of Iron Oxide Multicore Nanoflowers in Magnetic Hyperthermia and Photothermia. ACS Nano, inPress, 10.1021/acsnano.1c06212 . hal-03509995

HAL Id: hal-03509995
https://hal.sorbonne-universite.fr/hal-03509995v1

Submitted on 4 Jan 2022

Structure-Property-Function Relationships of Iron Oxide Multi-Core Nanoflowers in Magnetic Hyperthermia and Photothermia

Enzo Bertuit[†,‡], *Emilia Benassai*[†,‡], *Guillaume Mériguet*[†], *Jean-Marc Greneche*[+], *Benoit Baptiste*[#], *Sophie Neveu*[†], *Claire Wilhelm*[§] *and Ali Abou-Hassan*[†,*]

[†]Sorbonne Université, CNRS, PHysico-chimie des Électrolytes et Nanosystèmes InterfaciauX (PHENIX), F-75005 Paris, France

[+]Université du Maine, UMR CNRS 6283, Institut des Molécules et Matériaux du Mans (IMMM), Avenue Olivier Messiaen, 72085 Le Mans Cedex 9, France

[#]Sorbonne Université, UMR 7590 CNRS – Sorbonne Université – IRD-MNHN, Institut de Minéralogie, de Physique des Matériaux et de Cosmochimie (IMPMC), Case 115, 4 Place Jussieu, 75252 Paris Cedex 5, France

[§]PSL Research University − Sorbonne Université – CNRS, UMR168, Laboratoire PhysicoChimie Curie, Institut Curie, 75005 Paris, France

[‡]Both authors contributed equally

[*]Author to whom correspondence should be addressed:

ali.abou_hassan@sorbonne-universite.fr

Abstract

Magnetite and maghemite multi-core nanoflowers (NFs) synthesized using the modified polyol-mediated routes are to date among the most effective nano-heaters in magnetic hyperthermia (MHT). Recently, magnetite NFs have also shown high photothermal (PT) performances in the most desired second near infra-red (NIR-II) biological window making them attractive in the field of nanoparticle-activated thermal therapies. However, what makes magnetic NFs efficient heating agents in both modalities still remain an open question. In this work, we investigate the role of many parameters of the polyol synthesis on the final NFs size, shape, chemical composition, number of cores and crystallinity. These nanofeatures are later correlated to the magnetic, optical and electronic properties of the NFs as well as their collective macroscopic thermal properties in MHT and PT to find relationships between their structure, properties and function. We evidence the critical role of iron(III) and heating ramps on the elaboration of well-defined NFs with high number of multi-cores. While MHT efficiency is found to be proportional to the average number of magnetic cores within the assemblies, the optical responses of the NFs and their collective photothermal properties depend directly on the mean volume of the NFs (as supported by optical cross sections numerical simulations) and strongly on the structural disorder in the NFs, rather than the stoichiometry. The concentration of defects in the nanostructures, evaluated by photoluminescence and Urbach energy (E_U), evidences a switch in the optical behavior for a limit value of $E_U = 0.4$ eV where a discontinuous transition from high to poor PT efficiency is also observed.

Keywords

multi-core iron oxides, nanoflowers, magnetic nanoparticles, magnetic hyperthermia, photothermia, nanothermal agents, thermal therapies

Introduction

Due to their unique physico-chemical properties, multi-core iron oxide nanoparticles (NPs) also called nanoflowers (NFs), are used as functional materials in many applications,[1–4] including for diagnosis and therapy in the biomedical field.[5–8] NFs are efficient magnetic resonance imaging (MRI) contrast agents[9] and performant nano-heaters in magnetic hyperthermia (MHT), with specific loss powers (SLP) values amongst the highest reported ones for magnetic materials.[10,11] NFs efficiencies are explained by the presence of magnetic exchange couplings within the cores forming the flower-like assemblies, endowing them with enhanced magnetic relaxivity and susceptibility.[12] Because of a lower surface/volume ratio, NFs also present lower spin surface disorders when compared to single-core structures.[13] More recently, magnetic NFs have been proved to be promising materials for photothermal therapy (PTT) thanks to their absorption in the first[14] (around 808 nm for maghemite) and second[15] (around 1064 nm for magnetite) infra-red biological windows. However, how the fine structure features of NFs at the nanoscale govern their properties and their collective function in MHT and PT still needs to be elucidated.

As magnetic[16–18] and optical[19] properties of NPs directly rely on their size, shape, crystallinity and chemical composition, the control over the synthesis of NFs is of primary importance. Nevertheless, the understanding of the experimental synthesis parameters enabling the control of their formation is still scarce in literature.[20–22] To yield well-defined and monocrystalline magnetic NFs, different high temperature synthesis strategies have already been reported. For example, the so-called thermal decomposition of organometallic compounds (ACAC routes) results in the formation of hydrophobic NFs stable in diverse organic solvents.[23,24] Conversely, polyol-mediated syntheses, historically developed by Fievet, Lagier and Figlars,[25,26] provide hydrophilic NFs highly stable in aqueous media.[27,28] To induce the formation of flower-like structures by polyol processes, surfactants can be added in the reactive media or mixtures of different polyols can be used.[29,30] The influence of different synthesis parameters (temperature slope and heating time,[10] presence of water in the reaction mixture,[21] nature of polyol solvents,[31,32] proportions of iron precursors[33]) on the formation of iron oxide NFs has already been investigated but a clear overview is still missing.

Herein, in an attempt to rationalize the function of the NFs in MHT and PT and to understand the relationships between their structure at the nanoscale and their collective physical properties, we conducted a multi-scale materials science investigation ranging from a multi-parametric study of the synthesis parameters, their effect on the resulting NFs including their structure, electronic and magnetic properties to their heating function in MHT and PT as depicted in Scheme 1. First, the effect of heating conditions and iron precursor proportions on the resulting NP's characteristics including their morphology, size, stoichiometry, number and size of multi-cores, crystallinity are investigated. From the collective behavior of the resulting colloidal suspensions to the crystal defaults using the electronic structure as a fingerprint, NFs characteristics are fully analyzed at different length scales to establish correlations between the synthesis conditions responsible of their structure, their magnetic and optical properties and finally to their function in MHT and PT in order to understand what governs both modalities. We evidence the role of the synthesis conditions on the fine structure of the NFs including the number of cores and their size. We also demonstrate that the number of cores in the flower-like assemblies controls their magneto-thermal properties while the chemical stoichiometry and disorder defects govern their optical and photothermal behavior.

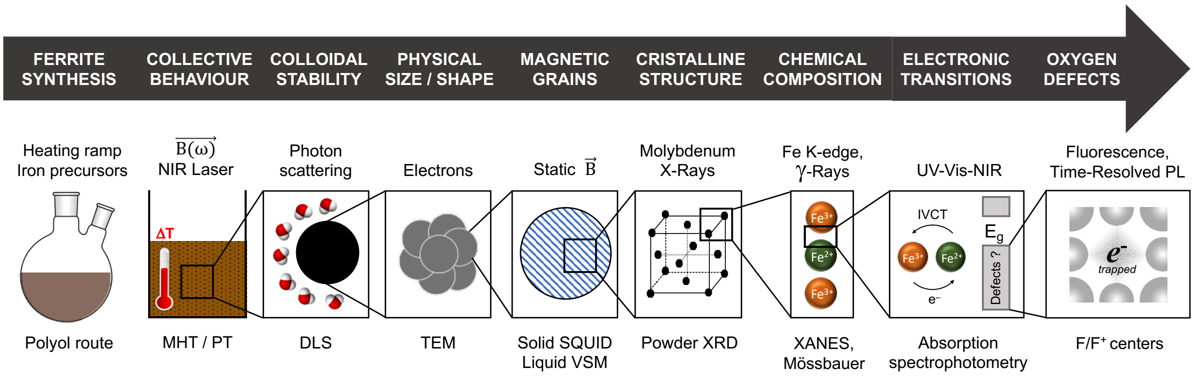

Scheme 1. Diagram summarizing the multi-scale materials-science approach used in this work, from the batch polyol synthesis of NPs and their collective behavior in colloidal suspensions to their sub-atomic level characteristics.

Results/Discussion

Effects of heating ramps, iron precursor molar ratios and oxidation on NFs morphology and composition

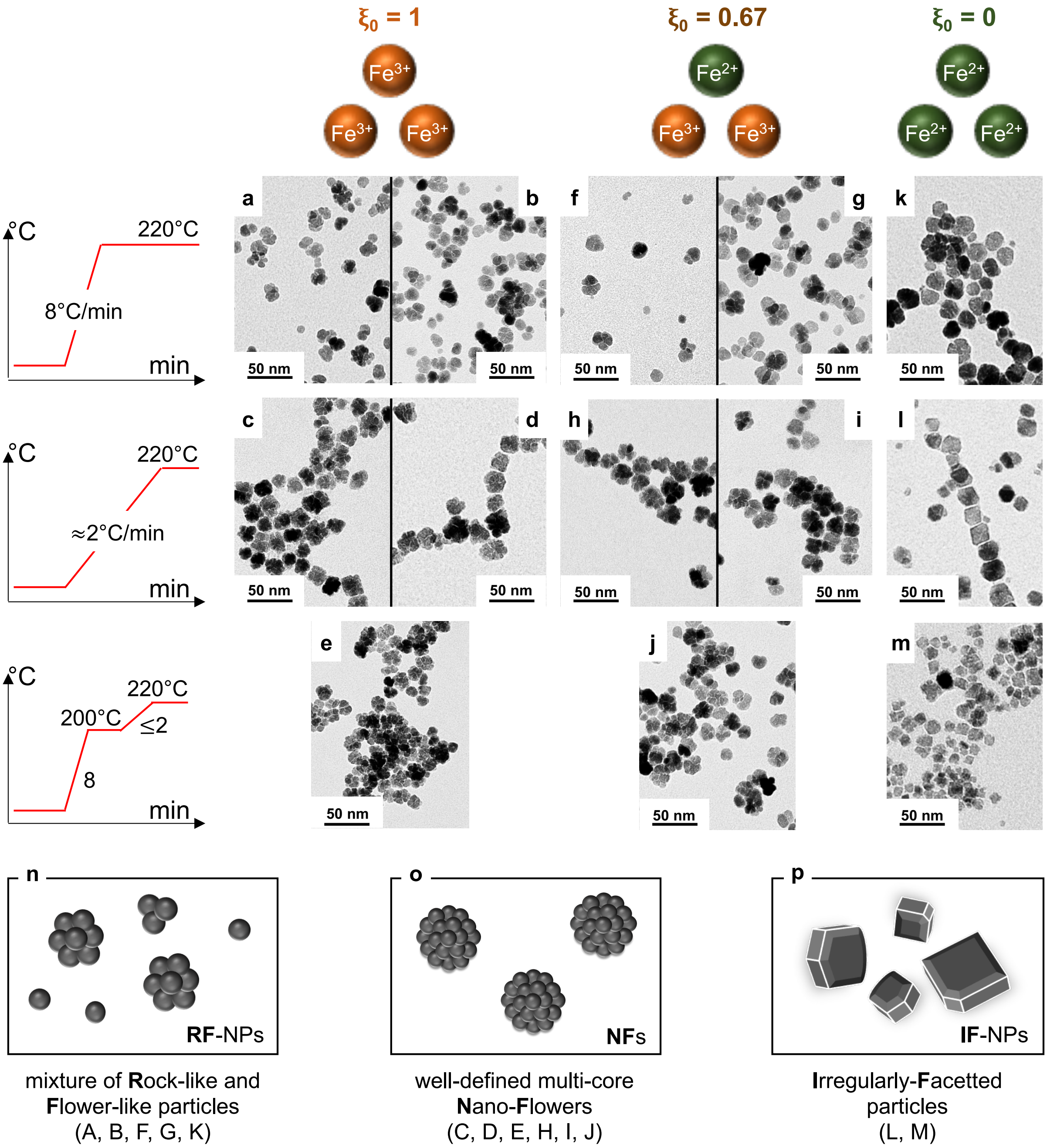

mixture of **R**ock-like and **F**lower-like particles (A, B, F, G, K)

well-defined multi-core **N**ano-**F**lowers (C, D, E, H, I, J)

Irregularly-**F**acetted particles (L, M)

Figure 1. a-m) Representative TEM micrographs (scale bars: 50 nm) of the synthetized iron oxide NPs for different heating conditions (lines) and iron precursor proportions ξ_0 =

$[Fe^{III}]/[Fe_{tot}]$ (columns). Each sample will be designated by the corresponding letter of this figure (see Table S1). n-p) Schematic description of the morphologies (RF-NPs, NFs, IF-NPs) of the obtained NPs. Letters in brackets indicate the morphology of each sample.

A complete morphological study was carried out in order to determine which synthesis parameters are best suited for the production of monodisperse and well-defined iron oxide NFs. Figure 1 shows representative TEM micrographs (see Figure S1 for size distribution histograms) of the NPs obtained for the different experimental conditions. Images are sorted by iron precursor ratios (columns) and heating ramps (lines, see Figure S2 for experimental temperature curves). In each column, different holding times (at 220°C) are also tested (1 hour for samples A, C, F, H, K, L; 2 hours for samples B, D, G, I; double plateau for samples E, J, M). Figures 1o–1p describe the three different shapes of the NPs observed in this work. Briefly, mixtures of Rock-like and Flower-like NPs (RF-NPs), well-defined multi-core Nano-Flowers (NFs) or Irregularly-Facetted NPs (IF-NPs) are obtained depending on the nature of the synthesis conditions. The use of a fast heating ramp of 8°C/min (FH) leads to RF-NPs, independently from the initial ratio of iron precursors. When the heating ramp is decreased to 2°C/min (SH) or split into a double heating ramp (DH: first 8°C/min followed by ≤2°C/min), NFs are obtained for $\xi_0 = 1$ and $\xi_0 = 0.67$. An exception is observed for $\xi_0 = 0$ syntheses (samples L and M) which surprisingly exhibit an IF-NP structure. Hemery *et al.*[21] demonstrated the importance of water for the successful elaboration of magnetic nanoflowers. Herein, despite an equal amount of water, no magnetic nanoflowers are observed if iron(II) is used as the only precursor ($\xi_0 = 0$) independently from the heating ramp. On the other side, when iron(III) or a mixture of iron(II) and iron(III) are used ($\xi_0 = 1$ or $\xi_0 = 0.67$), magnetic nanoflowers are obtained only for DH or SH ramps. These results show clearly that, in addition to the amount of water, the nature of the molecular precursors and heating ramps are important for the generation of nanoflowers by a modified polyol process. Based on recent findings by Gallo-

Cordova *et al.*[34] on the role of NMDEA in the elaboration of nanoflowers through the formation and stabilization of green rust phases (the intermediate products in magnetite formation), one may suppose the following. Green rust intermediates formed with iron(II) ($\xi_0 = 0$) are very unstable and evolve rapidly[35] to non-flower shaped structures through classical crystallization. It appears that the use of slow heating ramps is not sufficient to stabilize such intermediates, giving rise to the formation of IF-NPs only. Conversely, green rust intermediates generated in the presence of iron(III) ($\xi_0 = 1$ or $\xi_0 = 0.67$) are more stable and evolve by a slow nucleation resulting into small nanocrystals that can finally assemble into nanoflowers by oriented attachment. As a result, slow nucleation being favored by slow heating ramps, the formation and evolution of green rust intermediates could explain the higher yield in NFs observed for SH and DH when compared to FH ramps. These results clearly demonstrate that iron(III) is crucial for the formation of flower-like NPs and that the use of FH conditions favors the formation of undesired rock-like NPs. To further confirm these results, a synthesis with a very fast heating (VFH) ramp of 16.5°C/min (Sample N, see Figure S3) and one with a reverse double heating (RDH: first 2°C/min followed by 8°C/min) ramp (Sample O, see Figure S3) are carried out. The formation of spherical-like NPs is evidenced in the case of VFH while very well-defined NFs are obtained with RDH. The relative proportion of NFs and isolated rock-like NPs is evaluated from TEM micrographs for RDH (sample N), SH (samples D, I), DH (samples E), FH (samples B, G, K) and VFH (sample O) conditions. The proportion of NFs (see Figure S4) is found to decrease linearly with the mean heating ramp (2°C/min for DH, 1.3°C/min for RDH). Thus, the critical parameter controlling the yield in NFs is the mean heating ramp between 120°C and 220°C: the slower the ramp the higher the yield in NFs. The mean diameter (d_{TEM}) and polydispersity (σ_{TEM}) of the magnetic NPs (see Table S1) are found to depend on the applied heating ramps rather than the holding time or the precursor proportions. Excluding $\xi_0 = 0$ syntheses, FH ramps (samples A, B, F, G) yield average values of $< d_{TEM}^{FH} > = 15 \pm 1$ nm and $< \sigma_{\mathrm{TEM}}^{\mathrm{FH}} > = 0.30 \pm 0.05$ while both SH and DH ramps yield comparable results (samples C, D, H, I and E, J) with mean values of $< d_{\mathrm{TEM}}^{\mathrm{SH,DH}} > = 19 \pm 1$ nm and $< \sigma_{\mathrm{TEM}}^{\mathrm{SH,DH}} > = 0.24 \pm 0.01$. So, smaller and more polydisperse NPs are obtained with FH ramps when compared to SH and DH ramps. As SH and DH conditions present the same average heating ramps (2°C/min), we conclude again that heating conditions T = *f(t)* act as a thermodynamic state function: the critical parameter governing size and polydispersity is the average ramp between 120°C and 220°C rather than the nature of intermediate steps. As a result, the reaction time between 120°C and 220°C also conditions, in addition to the shape (proportion of NFs), the size and polydispersity of the resulting particles. Such results are in agreement with the work of Hugounenq *et al.*,[10] who obtained ≈20 nm NFs by applying a discontinuous multi-step heating ramp of 10°C/5min or a continuous heating of 2°C/min.

In order to investigate the effects of the chemical composition of the NPs on their magnetic and optical properties, a fraction of all samples is oxidized. TEM images of three randomly chosen samples (E, G and K; see Figure S5 for TEM micrographs and size distributions) show that morphology did not change after oxidation, while only minor size changes are observed with mean values of $< \Delta_{\mathrm{oxidation}}(d_{\mathrm{TEM}}) > = 1.7\%$ and $< \Delta_{\mathrm{oxidation}}(\sigma_{\mathrm{TEM}}) > = 15\%$ before and after the oxidation step. As surface state can also affect magnetic and optical properties,[36] the surface of the synthetized NPs is characterized by Fourier-Transform Infra-Red (FT-IR) spectroscopy on dried powders before and after oxidation for all samples. Identical spectral signatures are found for all samples with no significant changes before and after oxidation step (see Figure S6). The observed vibrations and stretching bands are in good agreement with previously reported spectra for acidic aqueous ferrofluids with NO_3^- counterions (see Table S2).[37]

The synthetized particles are analyzed by powder X-ray diffraction for crystalline phase identification. All samples are compatible with a spinel structure (see Figure S7a) characteristic of Fe_3O_4 or γ-Fe_2O_3 crystalline phases. A very small but significant shift of $\Delta_{2\theta} = 0.0152° \pm 0.001°$ towards higher angular values, corresponding to a small decrease of the lattice parameter, is observed for the set of oxidized samples by analyzing (220), (311) and (440) peak positions (see Figure S7b). These results suggest, as already reported, a higher oxidation state meaning a lower Fe^{II}/Fe^{III} ratio.[38–43] To quantify the stoichiometry of both non-oxidized and oxidized samples sets, XANES analyses (see Figures S8 and S9) are performed on some samples. Correction, normalization and analysis of the experimental raw data (Equations S1 to S5) are fully described in the supplementary information (see Figure S10).[44–51] Interestingly, the presence of iron(II) is found in the NPs even when the syntheses are carried out with iron(III) only ($\xi_0 = 1$). These results strongly suggest that DEG and/or NMDEA behave as *in situ* reducing agents of iron(III). Such hypothesis is reinforced by the detection inside the refluxing column of an aldehyde (oxidation product of alcohols) thanks to a silver mirror Tollens test (see Figure S11). At the same time, iron(III) is found for the syntheses starting from iron(II) only ($\xi_0 = 0$). No correlation is found between ξ_0 and R values and all samples are found to be off-stoichiometric magnetite (see Table S3). All these results highlight that NPs formation and stoichiometry control are involving complex processes that still need to be clarified. Upon oxidation of the NPs, iron(II) amount decreases in the structures reaching almost zero ($R \lesssim 0.05$) in most cases (see Table S3). To gain more insights on the distribution of magnetite and maghemite phases in the nanostructures, Mössbauer spectroscopy is performed at 77 K on representative samples C and C_{ox} (well-defined NFs). The spectra (see Figure S12) show different hyperfine structures with fairly well-defined magnetic sextets, typical of the presence of magnetically blocked NPs. Indeed, spectra of sample C_{ox} can be well described by means of two magnetic sextets while the one of sample C requires at least five components, in agreement with the presence of almost exclusively maghemite and a mixture of magnetite and maghemite, respectively. According to previous studies,[52,53] their proportions can be estimated from the mean value of the isomer shift (see Table S4), giving rise to 100 ± 1 % (sample C_{ox}, $< \delta_{iso} > = 0.455$ mm/s) of maghemite and 40 ± 3 % (sample C, $< \delta_{iso} > = 0.565$ mm/s) of maghemite (with the presence of Fe^{3+} and Fe^{2+} species, as well as intermediate oxidations state[54]). As shown from HR-TEM micrographs (see Figure S13), the NFs are almost perfect monocrystalline structures, with a very small angular mosaicity of 5.5 ± 0.2°. Assuming a magnetite-maghemite core-shell model[55] for the assembly ($d_{TEM} = 18.4$ nm for sample C), the NFs consist of a magnetite core of 9.6 nm diameter and a maghemite mean shell about 4.4 nm thick. Such a mixed structure agrees quite well with that observed with the spherical NPs prepared using ammonium R_4NOH alkaline agents with increasing aliphatic chain lengths (R = methyl, ethyl, propyl).[56] The reduction of the thickness of the shell when compared to spherical NPs can be explained by the nature of NPs aggregated into flower-like structures. Their densification prevents from the oxidation and thus the oxidized shell is smaller. As the synthesis pathways of all NPs are comparable, we can assume that all non-oxidized samples present a core-shell structure composed of a magnetite core and a small maghemite shell, while oxidized samples are mainly composed of maghemite.

Correlating the structure of the NFs to their function in magnetic hyperthermia

It has already been reported that multi-core NPs present enhanced magnetic properties when compared to single-core NPs, as surface disorder is drastically decreased.[12] The exchange coupling between the multi-core NPs also modifies the dynamic of the magnetic moments in a way that thermal losses are increased. As a result, saturation magnetizations and MHT efficiencies are often better for flower-like structures than for single-core NPs.[15] The magnetic properties of all samples are investigated in solid state under static magnetic field conditions and all samples show a superparamagnetic behavior (see Figure S14). The TGA-corrected saturation magnetization values (Equations S6 and S7, see Table S5) of non-oxidized and oxidized samples range around $M_S = 70 \pm 10$ emu/g_{mat}, consistent with previous reported values of ≈75 emu/g_{mat}[20] and ≈60 emu/g[57] and for Fe_3O_4/γ-Fe_2O_3 NFs and spheres, respectively. Evolution of magnetic properties with temperature is investigated by zero field cooled and field cooled (ZFC/FC) measurements (see Figure S15) to gain information about the blocking temperature (T_B) for samples with different shapes, diameters and oxidation states (D, E, G_{ox}, K_{ox}, M, M_{ox}). For all samples, T_B ranges between 180 K and 295 K (see Table S6) which confirms the superparamagnetic behavior of the NPs at ambient temperature. As previously reported, T_B is found to be higher in the case of multi-core NFs (D, E) and multi-core RF-NPs (G_{ox}, K_{ox}) when compared to single-core IF-NPs (M, M_{ox}). As diameters of investigated samples ranges between 13 and 24 nm, such a difference may not only be due to diameter differences but also to the presence of couplings between the grains in the multi-core assemblies. Before recording magnetization curves in liquid phase, the colloidal stability of all samples is evidenced by DLS and zeta potential measurements (see Table S7 and Figures S16, S17, S18). M–H curves allow the determination of the diameter of the magnetic cores[58] (d_m) assembled in the flower-like structures (see Figures S19, S20 and S21) thanks to a log-normal weighted Langevin law (Equations S8 to S12). In the case of RF-NPs and NFs, an average value of $< d_m > = 8.2 \pm 1$ nm (see Table S5) is found consistently with the value of 8 ± 1 nm obtained from HR-TEM micrographs, in good agreement with previously reported value of 8.4 ± 1.5 nm determined by HR-TEM by Lartigue *et al.*[12] Subsequently, the mean number of magnetic cores (N_{MC}) per NP is evaluated by comparing physical (d_{TEM}) and magnetic (d_m) diameters (see Tables S1 and S5). Assuming that NPs and magnetic cores are spherical, N_{MC} can be approximated as $N_{MC} = (d_{TEM}/d_m)^3$. At the same time, MHT experiments are carried out to measure the SLP of each sample (Equation S13, see Table S5) using an alternative magnetic field of H = 180 G operating at $f = 471$ kHz, to stay close to the safe domain of application of magnetic field ($H \cdot f_{\mathrm{lim}} = 5 \cdot 10^9$ A·m^{-1}·s^{-1}, $H \cdot f = 6.7 \cdot 10^9$ A·m^{-1}·s^{-1} here).[59] As shown in Figure 2a, non-oxidized and oxidized samples present the same N_{MC} values meaning that the oxidation process does not affect the multi-core structure. Moreover, N_{MC}(FH) is found to be significantly different (highly significative p-values < 0.001) from N_{MC}(SH) and N_{MC}(DH), which exhibit comparable results (non-significative p-value $\gg 0.05$). Briefly, FH ramps yield RF-NPs with a lower N_{MC} when compared to the NFs obtained with SH and DH ramps. More precisely, mean values of $< N_{\mathrm{MC}}^{\mathrm{FH}} > \approx 5$ and $< N_{\mathrm{MC}}^{\mathrm{SH}} > \approx < N_{\mathrm{MC}}^{\mathrm{DH}} > \approx 13$ are obtained for the three different heating conditions (SH, FH and DH). The number of magnetic cores is also determined for VFH (sample N) and RDH (sample O) conditions (see Figure S3) and yield $N_{\mathrm{MC}}^{\mathrm{VFH}} = 1.8$ and $N_{\mathrm{MC}}^{\mathrm{RDH}} = 23$. Figure 2b shows the dependence of N_{MC} value with the mean heating ramp. The number of magnetic cores is found to be inversely proportional to the mean ramp, which indicates that aggregation into flower-like structure is strongly favored by slow heating. N_{MC} values are finally plotted, for each sample, against the SLP obtained in MHT modality (Figure 2c). Two different regimes can be observed, characterized by SLP < 150 W/g_{Fe} for RF-NPs and SLP > 200 W/g_{Fe} for NFs. All SLP values are consistent with previously reported values for both NFs and RF-NPs when converted to field- and frequency-independent intrinsic loss power (ILP) values (see Figure S22 and Table S5). To the best of our knowledge, such a linear correlation between MHT efficiency and the number of cores in the flower-like assemblies has not been evidenced before. The linear correlation found here (Figure 2c) may be explained by an increase of exchange couplings between the cores. Indeed, as already reported,[60] the coupling energy can be written as:

$$E_{\mathrm{coupling}} = - \sum_{n=1}^{N_{\mathrm{MC}}} \sum_{k \neq n}^{N_{\mathrm{MC}}} J_{n,k} \cdot (\overrightarrow{S_n} \cdot \overrightarrow{S_k}) = - \sum_{n=1}^{N_{\mathrm{MC}}} \sum_{k \neq n}^{N_{\mathrm{MC}}} J_{n,k} \cdot S_n \cdot S_k \cdot \cos(\theta_{n,k}) \qquad (1)$$

where $J_{n,k}$ is the coupling constant between magnetic spins of core *n* (S_n) and core *k* (S_k) and decreases with the distance between S_n and S_k, and $\theta_{n,k}$ is the angle between the two magnetic spins S_n and S_k. According to Equation 1, a minimization of the coupling energy (*i.e.* a maximization of the exchange couplings) is obtained by maximizing N_{MC} and minimizing $\theta_{n,k}$ value. FFT analyses of HR-TEM micrographs show an average value of $< \theta > \sim 5.5°$. Since the NPs are almost monocrystalline, we assume that all $\theta_{n,k}$ can be approximated to $< \theta >$, so that all $\cos(\theta_{n,k})$ tend to 1. The coupling energy thus becomes a function of N_{MC} only. Consequently, the increase of MHT efficiency can be explained by the increase in the number of magnetic cores. Such results could help to the rationalized design of NFs with higher number of cores to maximize their heating efficiency in MHT modality by the use of very slow heating ramps.

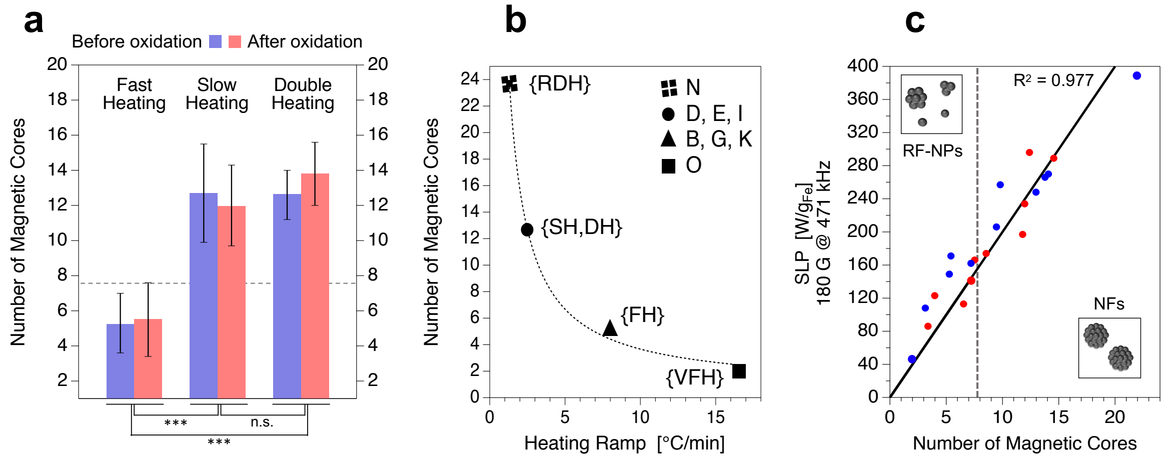

Figure 2. a) Number of magnetic cores for each type of heating condition before (blue) and after (red) the oxidization step (error bars: standard deviation of each series). Grey dashed line: N_{MC} border between RF-NPs and NFs. Significance of the *T*-tests between the different series are indicated below the histogram (∗∗∗ : *p*-value ≤ 0.001; n.s. : *p*-value > 0.05). b) Number of magnetic cores as a function of the mean heating ramp. Symbols: experimental points, dashed line: hyperbolic model ($R^2 = 0.987$). c) SLP in MHT as a function of N_{MC} for the non-oxidized

(blue) and oxidized (red) samples. Black solid line: linear model with a correlation coefficient of $R^2 = 0.977$. Grey dashed line: N_{MC} border between RF-NPs and NFs.

Relating the structure of the NFs to their optical properties and function in photothermia

Along with being highly efficient in MHT, we have recently shown that magnetite NFs are also performant nano-heaters in NIR-II mediated PT.[15] However, the reasons of their photothermal efficiency remained unclear. To rationalize the experimental optical data, we start by calculating the extinction spectra of stoichiometric Fe_3O_4 and γ-Fe_2O_3 NPs using an extension of the Mie theory[61,62] based on complex refractive index[63] values (see Figure S23 and Tables S8, S9). To do so, we assume that NFs can be approximated as perfectly spherical NPs. Calculations are performed for mean diameters ranging from 13 nm to 24 nm (Figures 3a–3d) to include all the experimental values listed in Table S1. The different codes used here are based on the Mie Python module developed by S. Prahl.[64] Codes are provided and fully described in the supplementary information (see Figures S24 and S25). Simulation of the scattering and the absorption parts of the extinction cross section for Fe_3O_4 and γ-Fe_2O_3 are shown in Figures 3a and 4b, respectively. When the diameter values are set to the extreme experimental diameters obtained by TEM (d_{min} = 13 nm and d_{max} = 24 nm), absorption is found to be the predominant phenomenon and scattering effects can be totally neglected even for the highest diameter. A different absorption signature is found for both stoichiometric magnetite (Figure 3c) and maghemite (Figure 3d) NPs, especially in the NIR-II region (1000–1400 nm) where an absorption band is evidenced for magnetite only. This absorption band can be assigned to an intervalence charge transfer (IVCT) between Fe^{3+} and Fe^{2+} cations which can only occur in magnetite.[61,65] We thus focus on the NIR-II region and more precisely around 1064 nm since it is a laser wavelength used in NIR-II mediated PT experiments.[66] For both magnetite and maghemite, the calculated extinction cross sections at 1064 nm are found to depend linearly on d_{TEM}^3 for a given polydispersity, and exponentially on the polydispersity for a given diameter (Figure 3e and 3f, respectively). The same behavior is observed for all the simulations independently from $\{d_{TEM}, \sigma_{TEM}\}$ values (see Figures S26, S27 and S28). These results demonstrate that optical responses are proportional to the mean volume (<V>) of a log-normal distribution of NPs. We thus define a morphological parameter corresponding to the third moment of a log-normal distribution $< V > = < d_{TEM}^3 > = d_{TEM}^3 \cdot \exp\left(\frac{9 \cdot \sigma_{TEM}^2}{2}\right)$ in order to linearize the optical responses with the physical shape. For a fixed $< V >$ value, the extinction cross section of magnetite at 1064 nm is ≈100 times higher than for maghemite.

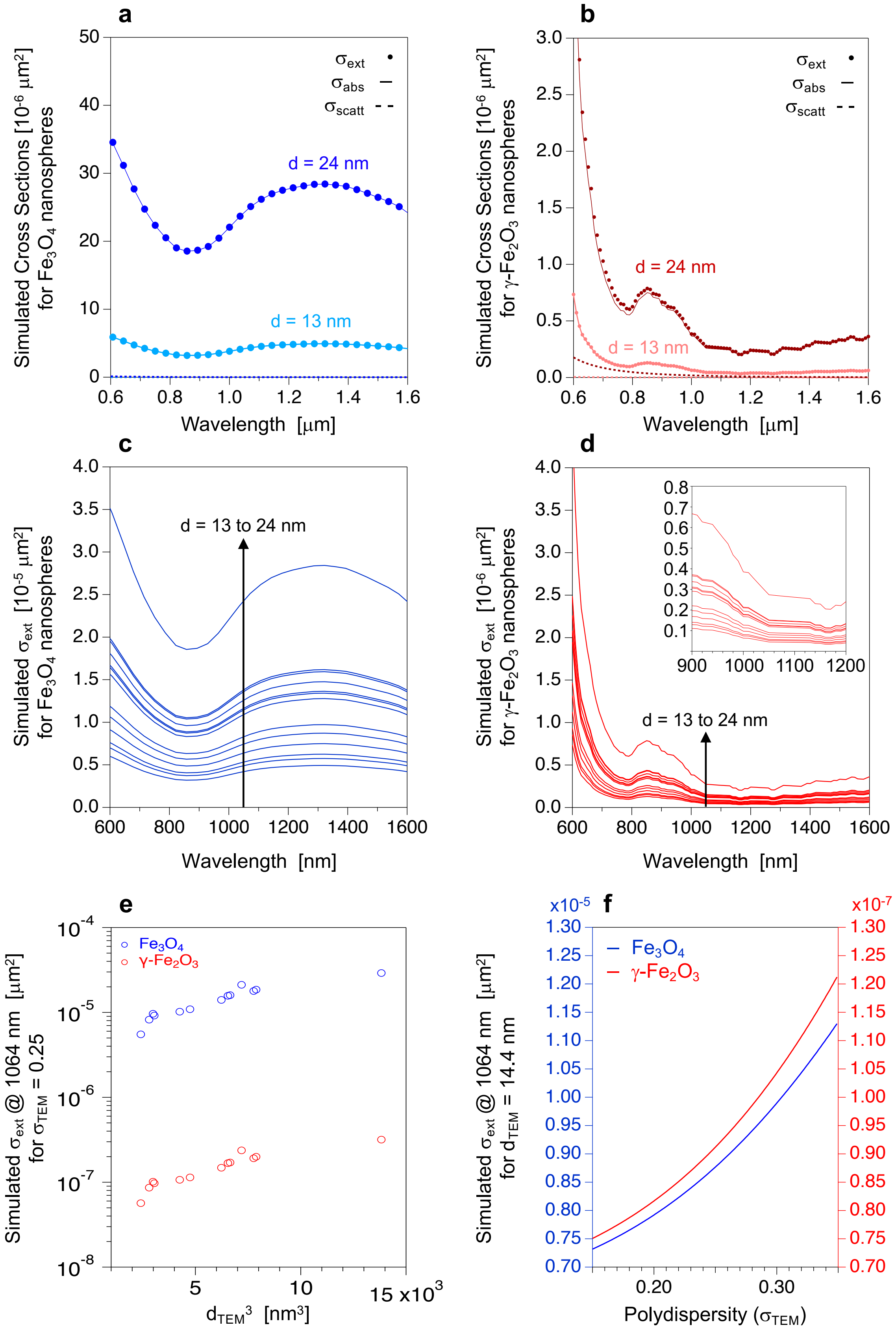
a
Simulated Cross Sections [10^{-6} µm2] for Fe_3O_4 nanospheres
σ_{ext} •
σ_{abs} —
σ_{scatt} - -
d = 24 nm
d = 13 nm
Wavelength [µm]
b
Simulated Cross Sections [10^{-6} µm2] for γ-Fe_2O_3 nanospheres
σ_{ext} •
σ_{abs} —
σ_{scatt} - -
d = 24 nm
d = 13 nm
Wavelength [µm]
c
Simulated σ_{ext} [10^{-5} µm^2] for Fe_3O_4 nanospheres
d = 13 to 24 nm
Wavelength [nm]
d
Simulated σ_{ext} [10^{-6} µm^2] for γ-Fe_2O_3 nanospheres
d = 13 to 24 nm
Wavelength [nm]
e
Simulated σ_{ext} @ 1064 nm [µm^2] for σ_{TEM} = 0.25
○ Fe_3O_4
○ γ-Fe_2O_3
d_{TEM}^3 [nm^3]
15 x10^3
f
x10^{-5}
x10^{-7}
— Fe_3O_4
— γ-Fe_2O_3
Simulated σ_{ext} @ 1064 nm [µm^2] for d_{TEM} = 14.4 nm
Polydispersity (σ_{TEM})

Figure 3. Simulated cross sections σ (extinction: points, absorption: solid lines, scattering: dotted lines) for spherical a) Fe_3O_4 NPs and b) γ-Fe_2O_3 NPs. Simulated extinction cross sections (σ_{ext}) as a function of wavelength for c) Fe_3O_4 NPs and d) γ-Fe_2O_3 NPs with diameters ranging from 13 to 24 nm. Simulated extinctions cross sections (σ_{ext}) around 1064 nm for e) different diameters at a given polydispersity of 0.25 and f) for different polydispersity at a given diameter of 14.4 nm.

The experimental particular extinction coefficient $\varepsilon_{exp}(NP)$ is deduced from the molar extinction coefficient $\varepsilon_{exp}(Fe)$ extracted from Beer-Lambert curves at 1064 nm (see Figure S29 and Table S10), according to Equations S14 and S15. In parallel, the theoretical particular extinction coefficient $\varepsilon_{theo}(NP)$ is deduced from the calculated extinction cross section (σ_{ext}) according to Equation S16. A comparison between $\varepsilon_{theo}(NP)$ and $\varepsilon_{exp}(NP)$ as a function of the mean volume $< V >$ is shown on Figure 4a. A good agreement is observed between the experimental and theoretical extinction coefficients for the set of non-oxidized samples, even if the stoichiometry of the sample deviated from the perfect stoichiometry considered in the simulations including low values around $R = 0.16$ (sample E). In the case of oxidized samples, experimental values deviate from the theoretical ones while their stoichiometry approaches the one of pure maghemite. The observed divergences may be due to intrinsic features of the NPs unrelated to stoichiometry and size which are not considered in the simulations. Indeed, factors such as shape imperfections, stoichiometry deviations or defects (vacancies and/or crystalline flaws)[67] may alter the electronic band structure of the NPs which in turn modify macroscopic material characteristics such as their optical properties.[68] As both non-oxidized and oxidized NPs present comparable flower-like structures, the observed deviations from simulations for the oxidized samples may not be attributed to the spherical shape assumed in the calculations. Similarly, both non-oxidized and oxidized samples are found to be off-stoichiometric with

$R_{non\text{-}ox} \neq R_{Fe_3O_4} = 0.5$ and $R_{ox} \neq R_{Fe_2O_3} = 0$ (Table S3). So, the disagreement between the experimental and theoretical data cannot be attributed to stoichiometric deviations either. Finally, the only remaining hypothesis for experimental deviations from calculations is the presence of intrinsic disorder in the NPs which influence the band structure of oxidized nanocrystals. To gain information about the semi-conductor band structure of the NPs, band-gap (E_g, see Figure S30 and Table S10) and Urbach (E_U, see Figure S31 and Table S10) energies are deduced from UV-Vis-NIR spectra according to Equations S17–S18 and S19, respectively. Both non-oxidized and oxidized samples present the same band-gap of $< E_{g_{non\text{-}ox}} > = 3.5 \pm 0.2$ eV and $< E_{g_{ox}} > = 3.4 \pm 0.2$ eV, which is close to the value of 3.1 eV reported by Fontjin *et al.*[63] As shown on Figure 4b, for the two sets of samples, $\ln[\varepsilon_{exp}(Fe)]$ linearly depends to $1/E_U$ as predicted by the Urbach theory (Equation S20). Interestingly, oxidized samples exhibit lower E_U values when compared to non-oxidized ones. The intensity of the IVCT is thus found to highly depend on the crystal defects: the higher the E_U, the higher the extinction coefficient at 1064 nm. As already reported, small E_U values correspond to high-defect systems[68–73] meaning that the conduction band shape of the oxidized samples is far from an ideal band. Consequently, differences between simulated and experimental data are explained by the presence of defaults in oxidized samples that are not considered in the calculations: defaults have a strong impact on the optical properties prevailing on stoichiometry. Focusing on non-oxidized NFs only, it is found that $\xi_0 = 1$ syntheses (samples C, D, E) yield higher E_U values when compared to $\xi_0 = 0.67$ syntheses (samples H, I, J) with mean values of $< E_U(C,D,E) > = 1.0 \pm 0.2$ eV and $< E_U(H,I,J) > = 0.6 \pm 0.1$ eV. It can thus be assumed that the use of iron(II) in the reactive medium generates less ordered structures than those obtained by an *in situ* polyol-mediated reduction of iron(III). Figure 4b also evidences two distinct areas separated from a limit value of $E_U = 0.4$ eV. Interestingly, when plotting ε_{exp} and E_U values of samples K_{ox} and M_{ox} (red stars) on Figures 4a and 4b they appear to belong to the region of the non-oxidized samples (blue areas) despite a low stoichiometry of R ≈ 0.16. Independently from stoichiometry, a switch in the optical behavior is observed for the limit value of $E_U = 0.4$ eV.

Figure 4c finally provides the PT efficiency at 1064 nm (see also Figure S32) through the SLP values as a function of concentration. These concentration dependent PT measurements are carried out in order to retrieve the light-to-heat conversion efficiency (η) values. All samples are characterized for two different concentrations ranging from 2 $\mathrm{mmol_{Fe}}$/L to 60 $\mathrm{mmol_{Fe}}$/L (see Tables S11, S12 and S13). The photothermal SLP of the non-oxidized samples (Figure 4c, blue circles and red stars) follows a light-to-heat conversion law (Equation S21) with an adjusted value of $< \varepsilon_{exp}(Fe) > =$ 115 $\mathrm{L{\cdot}mol_{Fe}^{-1}{\cdot}cm^{-1}}$ at 1064 nm, which is in the range of $\varepsilon_{exp}(Fe)$ values measured for these samples (between 64 and 207 $\mathrm{L{\cdot}mol_{Fe}^{-1}{\cdot}cm^{-1}}$). The light-to-heat efficiency extracted from this data analysis is equal to $\eta = 29\%$, which is in perfect agreement with the previously reported value of 30% for Fe_3O_4 materials.[74] The same adjustment is achieved for the oxidized samples but using $< \varepsilon_{exp}(Fe) > =$ 12 $\mathrm{L{\cdot}mol_{Fe}^{-1}{\cdot}cm^{-1}}$ at 1064 nm and results in a smaller value of $\eta_{ox} = 11\%$. Samples for which $\eta = 29\%$ are characterized by an average value of $< E_U > = 0.7 \pm 0.2$ eV while samples for which $\eta = 11\%$ present an average $< E_U > = 0.27 \pm 0.4$ eV. Consequently, one can deduce an E_U limit between 0.3 and 0.5 eV in agreement with the value of 0.4 eV extracted from Figure 4b.

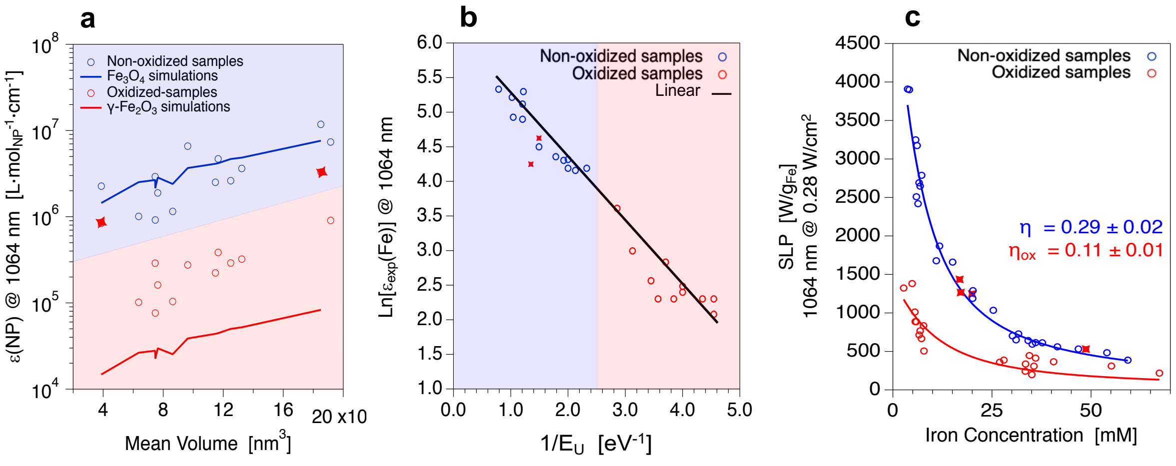

Figure 4. a) Comparison between experimental and theoretical NPs extinction coefficients at 1064 nm as a function of the mean volume of the log-normal distributions of NPs. b) Experimental molar extinction coefficients as a function of the inverse of Urbach energy (black solid line: linear model). c) SLP as a function of total iron concentration. Circles: experimental points, solid lines: fitting curve. Fe_3O_4 and γ-Fe_2O_3 data are systematically represented in blue and red, respectively. Red stars represent K_{ox} and M_{ox} samples that better fit within the set of non-oxidized samples.

Relating the structural defects of NPs to Urbach energy and photothermia

As established previously, structural defects have a direct impact on the optical properties of NPs and their function in PT, as translated by Urbach energy. In order to identify the nature of the defects and their proportions in the NPs, a complete photoluminescence study is carried out. The fluorescence emission spectra (Figure 5a) of all investigated samples show two different emission bands located around 525 nm and 590 nm for an excitation at 232 nm. The green emission at 525 nm can be ascribed to the presence of oxygen vacancies[75] within the spinel structures. Under irradiation of 232 nm, the created photo-excited holes (h^*) can combine with electrons trapped in singly-ionized ($O_O^x \sim V_O^+ + e^-_{trapped}$) or uncharged ($O_O^{2-} \sim V_O^x + 2e^-_{trapped}$) oxygen vacancies, respectively called F^+-centers and F-centers. The subsequent deexcitation of electron-hole combinations gives rise to the emission of different photons according to the following reactions:

$$O_O^x + h\nu_{abs}(232\text{ nm}) \rightarrow V_O^+ + e^-_{trapped} + h^* + \tfrac{1}{2}O_2 \rightarrow O_O^x + h\nu_{em}(F^+\text{-centers}) \qquad (2)$$

$$O_O^{2-} + h\nu_{abs}(232\text{ nm}) \rightarrow V_O^x + 2e^-_{trapped} + 2h^* + \tfrac{1}{2}O_2 \rightarrow O_O^{2-} + h\nu_{em}(F\text{-centers}) \qquad (3)$$

where the Kröger-Vink[76] notation for defects is used and hν represents an absorbed (abs) or emitted (em) photon. The green emission is expected to be composed of two different contributions if both F and F^+ centers are present in the nanomaterial. The yellowish emission around 590 nm is usually ascribed to the presence of interstitial oxygen defects.[77] To gain insights on the nature of defects present in the NPs, fluorescence emission spectra are modeled by the convolution of several gaussian functions (see Figure S33). In all cases, three distinct components centered around 520 nm, 532 ± 2 nm and 590 nm are found. According to previous works,[75,77] these contributions can be ascribed to F^+-centers (Equation 2), F-centers (Equation 3) and interstitial oxygen defects, respectively. The proportions of each defect within the nanostructures are estimated thanks to the area of each gaussian function (see Table S14).[78] Briefly, the amount of interstitial oxygen defects is found to be constant in the investigated samples with a mean percentage of 23 ± 2 %. The relative proportion of the two types of F-centers (F/F^+ ratio) ranges between 1.5 and 3.1 depending on the sample, for which synthesis conditions are not identical (variation of heating ramps or iron precursor proportions). Such results are consistent with the fact that the proportion and nature of F-centers highly depend on the history of the materials.[79] Time-resolved photoluminescence spectroscopy is carried out for an excitation at 232 nm. Emission wavelengths of 525 nm and 590 nm are investigated to obtain fluorescence lifetimes of the different excited states. For all samples, the decay at 525 nm (Figure 5b) are modeled by a bi-exponential function (Equation S22) suggesting two different modes of deexcitation which are heterogeneously distributed.[14] Such results are consistent with the previously evidenced presence of both F and F^+-centers. Mean values of $\tau_1 = 29 \pm 2$ µs and $\tau_2 = 4.6 \pm 0.5$ µs with relative proportions (Equation S23)[80] of 64 ± 5 % and 36 ± 5 % are found. As evidenced by emission spectra, F-centers are more abundant so one can assume that $\tau_1 = \tau_{F\text{-centers}}$ and $\tau_2 = \tau_{F+\text{-centers}}$. All results are listed in Table S15 and are consistent with previously reported values in the microseconds range for spinel nanomaterials.[76] Fluorescence decays at 590 nm (Figure 5c) also present two exponential contributions ($\tau_1 = 14 \pm 1$ µs, $\tau_2 = 1.9 \pm 0.3$ µs) suggesting the presence of two types of interstitial oxygen defects. As surface excited states are known to present very fast decays and NFs present low surface/volume ratios, the relative proportion of the lifetimes (68 ± 5 % for τ_1 and 32 ± 5 % for τ_2) and the fastness of the second component allow to ascribe the deexcitations to core ($\tau_1 = \tau_{core}$) and surface ($\tau_2 = \tau_{surf}$) oxygen defects respectively. Finally, the integrated fluorescence intensity is plotted against the characteristic defect value $1/E_U$ (Figure 5d). A good correlation between the concentration of emitting defects and $1/E_U$ values is observed. The experimental points are modeled by a power law evidencing a linear dependence of the fluorescence with E_U^4 (Figure 5d, inset) which means that defect concentration strongly enhances the fluorescence intensity. A linear increase of integrated fluorescence with $1/E_U$ is evidenced at small values followed by a plateau at $1/E_U = 2.5$ eV^{-1} ($E_U = 0.4$ eV). Such limit corresponds to the previously determined Urbach limit value for absorption and PT efficiency (ε and η, respectively) which means that NPs presenting high level of fluorescence are less efficient in PT. It has already been proved that electronic hoping along the Fe^{III}–O–Fe^{II} chain is decreased by high concentrations of oxygen vacancies.[81,82] So, the decrease of PT efficiency in the case of highly fluorescent samples may be explained by a diminution of the electron transfer between Fe^{II} and Fe^{III} (IVCT) when oxygen vacancies are abundant, giving rise preferentially to phonon-mediated non-radiative deexcitations.

.

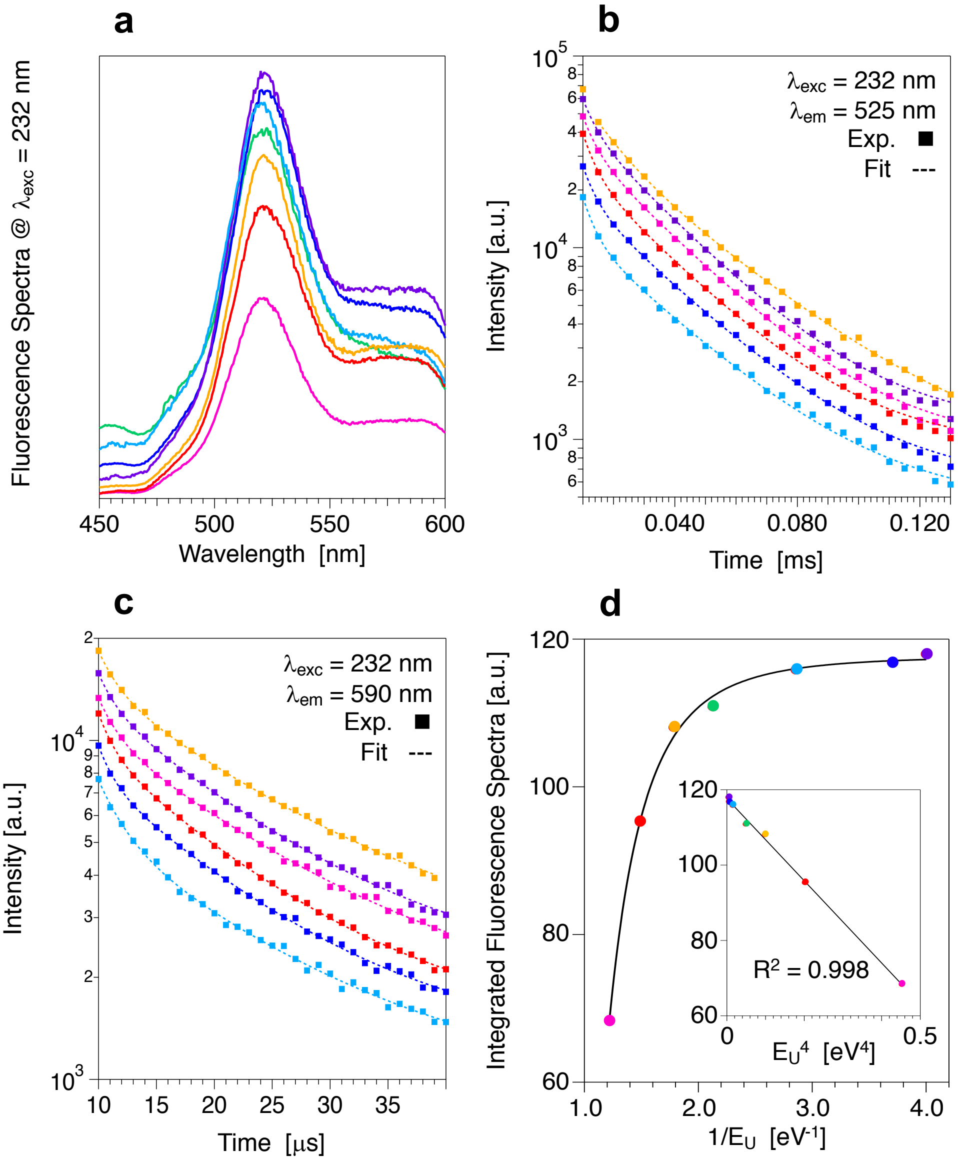

Figure 5. a) Fluorescence emission spectra recorded for an excitation wavelength of 232 nm. b,c) Time-resolved photoluminescence spectra measured for an excitation wavelength of 232 nm with an emission at b) 525 nm and c) 590 nm. Squares: experimental points, dashed lines: bi-exponential decay models. d) Plot of the integrated fluorescence spectra between 450 nm and 600 nm against the characteristic defect values $1/E_U$ modeled by a power law (black solid line). The inset shows de linear dependence of the integrated fluorescence spectra with E_U^4 ($R^2 = 0.998$). Color code: B (green), E_{ox} (blue), G (orange), I (red), I_{ox} (purple), L (pink) and L_{ox} (blue).

Conclusions

In this work, we investigated the effects of polyol synthesis parameters such as heating ramps, iron precursor molar ratios and oxidation step on flower-like multi-core NPs (NFs) in terms of size, shape, chemical composition and crystallinity. We then correlated their nano-structure characteristics to both magnetic and optical properties, including magnetic hyperthermia (MHT) and photothermia (PT), the leading NPs-based modalities for thermal therapy of cancer. Firstly, we established that iron(III) is a crucial actor for the formation of well-defined NFs in the polyol process while iron(II) is not necessary. The experimental heating conditions are found to control the morphology of the resulting NPs with fast ramps yield smaller, more polydisperse and poorly defined flower-like NPs, while slow ramps produce larger and well-defined NFs. Comparing SH and DH ramps, we point out that the mean heating ramp between 120°C and 220°C was the key parameter that govern the flower-like structure formation. A linear correlation was then established between MHT efficiencies and the number of magnetic cores composing the flower-like assemblies. Such linear relationship must be attributed to an increase of exchange coupling between the cores. Conversely, the optical properties are found to depend linearly on the mean volume of the NPs and strongly on the crystal defects rather than the stoichiometry. When focusing on E_U values, it was evidenced that iron(III)-based syntheses yield less disordered structures when compared to the iron(II,III)-based syntheses. Moreover, a switch in the optical behavior is observed for the limit value of $E_U = 0.4$ eV independently from stoichiometry, explaining the differences of optical properties between the samples. The same limit value of E_U is observed for PT efficiencies when comparing SLP between the different sets of samples. Such a E_U limit value was also confirmed by fluorescence measurements establishing the crucial role of defects on the optical properties of NPs and their efficiency in PT. These results suggest that optimal MHT and PT efficiency can be reached for large volume NFs composed of a high number of cores having low concentration of defects. Such nanostructures can be obtained with the modified polyol route by the use of iron(III) only (decrease of defects) and very slow temperature ramps (increase of the number of cores). To date available literature on iron oxide clusters have mainly focused on understanding the magnetic properties of NFs from the side of magnetism or more recently by structural analysis (using high resolution TEM techniques) but at the level of one single NP. In addition, and to the best of our knowledge, the photothermal properties rationalization and correlation at multiple bottom-up levels was never attempted. Taken together, these results will help rationalizing the design of efficient nano-heaters for thermal therapies.

Methods/Experimental

Chemicals. *N*-methyldiethanolamine (NMDEA, >99%), diethylene glycol (DEG, >99%), iron(III) chloride hexahydrate ($FeCl_3 \cdot 6H_2O$, 99%) and iron(II) chloride tetrahydrate ($FeCl_2 \cdot 4H_2O$, 99%) are purchased from Merck. Sodium hydroxide pellets (NaOH, 99%), hydrochloric acid (HCl, 37%), iron(III) nitrate nonahydrate ($Fe(NO_3)_3 \cdot 9H_2O$, >96%), ethanol (96%), nitric acid (HNO_3, 68%), acetone (>99%), diethyl ether (Et_2O, 100%) and silicon oil (47-V-350) are purchased from VWR International. All chemicals are used without further purification.

Synthesis procedures. Iron(II,III)-based syntheses (ξ_0 = 0.67): in a typical experiment, $FeCl_3 \cdot 6H_2O$ (1.08 g, 4 mmol, 2 eq.) and $FeCl_2 \cdot 4H_2O$ (0.39 g, 2 mmol, 1 eq.) are dissolved overnight in a mixture of DEG (40 mL) and NMDEA (40 mL) under N_2 inert atmosphere. At the same time, NaOH pellets (0.64 g, 16 mmol, 8 eq.) are grinded and dissolved overnight in a mixture of DEG (20 mL) and NMDEA (20 mL). After 30 min under N_2 inert atmosphere, the two solutions are mixed by magnetic stirring for 1 hour still under N_2 inert atmosphere. 500 μL of ultra-pure water are added and the resulting solution is then heated at 220°C (reflux) thanks to a silicon oil bath. The solution is finally allowed to cool down to room temperature. The black suspensions are diluted in ethanol to be magnetically separated and washed as follow: one time in diluted HNO_3 (10%) for ten minutes, two times in acetone and two times in Et_2O. The black solid is then re-dispersed in a minimum of ultra-pure water to obtain a stable aqueous ferrofluid. Iron(III)-based syntheses ($\xi_0 = 1$): iron(II) precursor is replaced by iron(III) precursor (1.62 g, 6 mmol). The dissolution of iron(III) salts into polyols takes place in half an hour instead of one night for the iron(II,III) mixture and the same procedure described before is performed under oxic conditions. Iron(II)-based syntheses ($\xi_0 = 0$): iron(III) precursor is replaced by iron(II) precursor (1.19 g, 6 mmol) and the same procedure as iron(II,III)-based syntheses is performed. Heating conditions: different heating conditions are investigated for each ξ_0 value thanks to a silicon oil bath placed on a Cat MCS 77 heating plate equipped with a thermocouple, allowing a precise control of the temperature over time. The temperature variations inside the reactive medium are recorded as a function of reaction time using an USB-connected (EL-USB-TC-LCD, Thermocouple Data Logger) thermometer. Briefly, heating speeds of 480°C/h and 120°C/h are set to carry out the fast heating ramp (FH) conditions of 8°C/min and the slow heating ramp (SH) conditions of 2°C/min, respectively. Once the temperature reaches ≈220°C, it is hold stable for durations of 1 hour and 2 hours. In the case of double heating ramp (DH) conditions, the first heating speed is set at 480°C/h until the temperature reaches 200°C (plateau of 50 min) and switched to 120°C/h to go from 200°C to 220°C (plateau of 60 min). In the case of reverse double heating (RDH), the first heating speed is set at 120°C/h until the temperature reaches 200°C (plateau of 50 min) and switched to 480°C/h to go from 200°C to 220°C (plateau of 60 min). Very fast heating (VFH) ramp of 16.5°C/min is obtained by setting the speed to 1000°C/h until the temperature of 220°C is reached (plateau of 60 min). Oxidation step ($Fe_3O_4 \rightarrow \gamma\text{-}Fe_2O_3$): 323 g of the oxidation agent

$Fe(NO_3)_3{\cdot}9H_2O$ (oxi) are dissolved in 800 mL of ultra-pure water under magnetic stirring and heated until ebullition. In parallel, a volume V_{FF} of ferrofluid is precipitated in a volume $3V_{FF}$ of HNO_3 (10%) on a permanent magnet to remove the supernatant. A precise volume V_{oxi} (Equation 4) of the boiling oxidation agent solution is then added on the precipitated NPs to respect a constant ratio β equal to 3 (Equation 5).

$$V_{oxi} = \frac{[Fe]_{FF} \cdot V_{FF}}{3 \cdot [oxi]} \qquad (4)$$

$$\beta = \frac{n_{oxi}(Fe)}{n_{FF}(Fe)} \equiv 3 \qquad (5)$$

The resulting solution is magnetically stirred and maintained at 75°C for 30 minutes before being allowed to cool down to room temperature. The classical washing procedure described before is finally followed to obtain an oxidized aqueous ferrofluid.

Characterizations. The morphology of the NPs is imaged using a JEOL-1011 transmission electron microscope operating at 100 kV. Size distributions are determined thanks to Image J software by measuring manually 300 NPs on at least three different images. The resulting histograms are modelized by a log-normal law using Igor Pro 7 software to determine the mean physical diameter (d_{TEM}) and the polydispersity (σ_{TEM}) of each sample. High-resolution TEM (HR-TEM) is performed on a JEOL 2010 operating at 200 kV. The total iron concentrations of NPs suspensions are measured by atomic absorption spectroscopy (AAS, PinAAcle 500, Perkin Elmer) and/or induced-coupled plasma atomic emission spectroscopy (ICP-AES, iCAP 6500, Thermo) by degrading the samples in concentrated HCl (37%) before a dilution in HNO_3 (2%). Dynamic light scattering and zeta potential measurements are performed on a Malvern Zetasizer Nano-ZS. Samples are studied in water at room temperature using a back-scattering angle of 173°. Fourier-Transform Infra-Red (FT-IR) spectroscopy is performed on a Bruker TENSOR 27 spectrophotometer with a resolution of 4 cm^{-1} between 400 cm^{-1} and 4000 cm^{-1}

on dried powders diluted in solid KBr. Magnetization hysteresis loops in liquid phase are measured using a home-made vibrating sample magnetometer in the range -9 kOe to +9 kOe. Zero field cooled and field cooled measurements (ZFC/FC) are performed on frozen colloidal suspensions between 10 K and 275 K with an applied field of 50 Oe on a Quantum Design PPMS equipped with a VSM module. Magnetization curves in solid phase (powder) are measured on a MPMS-XL7 Quantum Design SQUID in the range 0 Oe to 25 kOe. Thermogravimetric analyses (TGA) are performed on a TA TGA550 Discovery series operating in high-resolution mode with a heating speed of 20°C/min in the range 20°C–600°C. MHT experiments are carried out using 0.5 mL Eppendorf® containing 50 µL of the NPs suspensions excited for 600 seconds by an alternating magnetic field generator device (DM3, NanoScale Biomagnetics) operating at 180 Gauss with a frequency of 471 kHz (temperature increase is measured by an infrared camera FLIR SC7000). X-Ray powder diffraction measurements are carried out at the XRD platform of the IMPMC (Paris, France) on a Rigaku MM007HF diffractometer equipped with a Mo rotating anode source ($\lambda K_{\alpha 1}$ = 0.709319 Å, $\lambda K_{\alpha 2}$ = 0.713609 Å), Varimax focusing optics and a RAXIS4++ image plate detector. The detector is installed at a distance of 200 mm and the beam size fixed to 100 µm. From samples in 0.3 mm borosilicate capillaries, the XRD powder patterns are collected from $2\theta = 2°$ to $2\theta = 45°$ during 30 min at 20°C. LaB_6 standard sample is measured in the same experimental conditions to calibrate the FIT2D program, the image processing software used to integrate the intensities around the Debye−Scherrer rings and to get the 1D patterns. The crystal structure refinements are carried out using the Rietveld method as implemented in the FullProf software (Rodriguez-Carvajal, 1993). Starting from the known cell parameters of maghemite, the refinements converge rapidly. The peak widths are significantly larger than the instrumental resolution ($2\theta \sim 0.15°$). Starting from the instrumental resolution function, anisotropic size parameters are refined. It improves significantly the fits and allows to extract the size of mean coherent domains which are found to be almost spherical. X-ray absorption spectroscopy at Fe K-edge is performed at Synchtoron SOLEIL on the ROCK line in 1 mm diameter glass capillary, using a Si(111) monochromator. ^{57}Fe transmission Mössbauer spectra are obtained using a conventional constant acceleration transducer and a ^{57}Co source diffused into a Rh matrix. The experiments are performed at 77 K using a bath cryostat on samples resulting from frozen solutions containing approximately 3 mg_{Fe}/cm^2. The spectra are analyzed using a least-squares fitting method involving Lorentzian functions while the values of isomer shift are referred to that of α-Fe at 300 K. UV-Vis-NIR spectra (400–1100 nm) are recorded at room temperature in a 1 cm quartz cuvette using an Avantes spectrophotometric set-up composed of an AvaLight-DHc lamp connected by optical fibers to a StarLine AvaSpec UV/Vis detector and to a NIRLine AvaSpec-NIR256-1.7 NIR detector. Infrared PT experiments are carried out using 0.5 mL Eppendorf® containing 50 µL of the NPs suspensions excited for 300 seconds by a NIR laser (1064 nm, 0.28 W/cm^2) coupled to an optical fiber from Laser Components SAS (temperature increase was measured by an infrared camera FLIR SC7000). Fluorescence emission spectra are recorded on a Cary VARIAN Eclipse fluorescence spectrophotometer in 1 cm quartz cuvette with a excitation wavelength of 232 nm, a resolution of 1 nm/s and slits of 20 nm for both emission and excitation. Time-resolved fluorescence spectroscopy measurements are obtained using a Jobin-Yvon Fluorolog 3 Fluorometer equipped with a UV-Xenon flash tube. Excitation is set at 232 nm with 14 nm slits in both emission and excitation. Sample window and initial delay are set to 0.05 and 0.01, respectively. Two emission wavelengths (525 and 590 nm) are investigated with increments of 0.005 (525 nm) and 0.001 (590 nm).

Associated content

Supporting Information

The supporting Information is available free of charge *via* the Internet at:

Theoretical basis and equations, additional figures including TEM and HR-TEM, size distributions histograms, powder XRD diffraction data and Rietveld refinements, XANES data, ^{57}Fe Mössbauer spectra, SQUID, TGA, ZFC/FC measurements and DLS measurements, ILP values, Python codes, Beer-Lambert plots at 1064 nm, Urbach and Tauc plots, MHT and PT measurements, fluorescence emission spectra and additional tables.

Author Information

Corresponding Author

Ali Abou-Hassan Sorbonne Université, CNRS, PHysico-chimie des Électrolytes et Nanosystèmes InterfaciauX (PHENIX), F-75005 Paris, France. ali.abou_hassan@sorbonne-universite.fr

Author contributions

The manuscript was written through contributions of all authors. All authors have given approval to the final version of the manuscript.

Acknowledgments

E. Bertuit and A. Abou-Hassan acknowledge the doctoral school ED388 for funding. We acknowledge the support of the French Agence Nationale de la Recherche (ANR) under reference ANR-18-CE09-0004 (MicroNanoCell project). The authors acknowledge the staff of the MPBT (physical properties – low temperature) platform of Sorbonne Université for their support. The authors would also like to thank Dr. Anne-Laure Rollet and Dr. Juliette Sirieix-

Plénet for X-ray absorption measurements at Synchrotron SOLEIL. We acknowledge SOLEIL for provision of synchrotron radiation facilities and we would like to thank Valérie Briois for assistance in using beamline ROCK. The authors thank Dr. Hélène Brault (IMJR, Université de Nantes) and Dr. Nicolas Menguy (IMPMC, Sorbonne Université) for their assistance during time-resolved fluorescence and HR-TEM measurements. The authors also thank Aude Michel-Tourgis, Delphine Talbot (PHENIX, Sorbonne Université) and Laure Cordier (IPGP, Université de Paris) for iron concentration measurements by AAS or ICP-AES.

References

(1) Stanković, D. M.; Ognjanović, M.; Espinosa, A.; del Puerto Morales, M.; Bessais, L.; Zehani, K.; Antić, B.; Dojcinović, B. Iron Oxide Nanoflower–Based Screen Print Electrode for Enhancement Removal of Organic Dye Using Electrochemical Approach. *Electrocatalysis* **2019**, *10* (6), 663–671. https://doi.org/10.1007/s12678-019-00554-1.

(2) Han, J.; Luo, P.; Wang, L.; Li, C.; Mao, Y.; Wang, Y. Construction of Magnetic Nanoflower Biocatalytic System with Enhanced Enzymatic Performance by Biomineralization and Its Application for Bisphenol A Removal. *J. Hazard. Mater.* **2019**, *380*, 120901. https://doi.org/10.1016/j.jhazmat.2019.120901.

(3) Moyano, A.; Serrano-Pertierra, E.; Salvador, M.; Martínez-García, J.; Piñeiro, Y.; Yañez-Vilar, S.; Gónzalez-Gómez, M.; Rivas, J.; Rivas, M.; Blanco-López, M. Carbon-Coated Superparamagnetic Nanoflowers for Biosensors Based on Lateral Flow Immunoassays. *Biosensors* **2020**, *10* (8), 80. https://doi.org/10.3390/bios10080080.

(4) Urraca, J. L.; Cortés-Llanos, B.; Aroca, C.; Presa, P. de la; Pérez, L.; Moreno-Bondi, M. C. Magnetic Field-Induced Polymerization of Molecularly Imprinted Polymers. *J. Phys. Chem. C* **2018**, *122* (18), 10189–10196. https://doi.org/10.1021/acs.jpcc.7b12804.

(5) Pelaz, B.; Alexiou, C.; Alvarez-Puebla, R. A.; Alves, F.; Andrews, A. M.; Ashraf, S.; Balogh, L. P.; Ballerini, L.; Bestetti, A.; Brendel, C.; Bosi, S.; Carril, M.; Chan, W. C. W.; Chen, C.; Chen, X.; Chen, X.; Cheng, Z.; Cui, D.; Du, J.; Dullin, C.; Escudero, A.; Feliu, N.; Gao, M.; George, M.; Gogotsi, Y.; Grünweller, A.; Gu, Z.; Halas, N. J.; Hampp, N.; Hartmann, R. K.; Hersam, M. C.; Hunziker, P.; Jian, J.; Jiang, X.; Jungebluth, P.; Kadhiresan, P.; Kataoka, K.; Khademhosseini, A.; Kopeček, J.; Kotov, N. A.; Krug, H. F.; Lee, D. S.; Lehr, C.-M.; Leong, K. W.; Liang, X.-J.; Ling Lim, M.; Liz-Marzán, L. M.; Ma, X.; Macchiarini, P.; Meng, H.; Möhwald, H.; Mulvaney, P.; Nel, A. E.; Nie, S.; Nordlander, P.; Okano, T.; Oliveira, J.; Park, T. H.; Penner, R. M.; Prato, M.; Puntes, V.; Rotello, V. M.; Samarakoon, A.; Schaak, R. E.; Shen, Y.; Sjöqvist, S.; Skirtach, A. G.; Soliman, M. G.; Stevens, M. M.; Sung, H.-W.; Tang, B. Z.; Tietze, R.; Udugama, B. N.; VanEpps, J. S.; Weil, T.; Weiss, P. S.; Willner, I.; Wu, Y.; Yang, L.; Yue, Z.; Zhang, Q.; Zhang, Q.; Zhang, X.-E.; Zhao, Y.; Zhou, X.; Parak, W. J. Diverse Applications of Nanomedicine. *ACS Nano* **2017**, *11* (3), 2313–2381. https://doi.org/10.1021/acsnano.6b06040.

(6) Ognjanović, M.; Radović, M.; Mirković, M.; Prijović, Ž.; Puerto Morales, M. del; Čeh, M.; Vranješ-Đurić, S.; Antić, B. ^{99m} Tc-, ^{90} Y-, and ^{177} Lu-Labeled Iron Oxide

Nanoflowers Designed for Potential Use in Dual Magnetic Hyperthermia/Radionuclide Cancer Therapy and Diagnosis. *ACS Appl. Mater. Interfaces* **2019**, *11* (44), 41109–41117. https://doi.org/10.1021/acsami.9b16428.

(7) Curcio, A.; Silva, A. K. A.; Cabana, S.; Espinosa, A.; Baptiste, B.; Menguy, N.; Wilhelm, C.; Abou-Hassan, A. Iron Oxide Nanoflowers @ CuS Hybrids for Cancer Tri-Therapy: Interplay of Photothermal Therapy, Magnetic Hyperthermia and Photodynamic Therapy. *Theranostics* **2019**, *9* (5), 1288–1302. https://doi.org/10.7150/thno.30238.

(8) Van de Walle, A.; Perez, J. E.; Abou-Hassan, A.; Hémadi, M.; Luciani, N.; Wilhelm, C. Magnetic Nanoparticles in Regenerative Medicine: What of Their Fate and Impact in Stem Cells? *Mater. Today Nano* **2020**, *11*, 100084. https://doi.org/10.1016/j.mtnano.2020.100084.

(9) Hu, F.; MacRenaris, K. W.; A. Waters, E.; Schultz-Sikma, E. A.; Eckermann, A. L.; Meade, T. J. Highly Dispersible, Superparamagnetic Magnetite Nanoflowers for Magnetic Resonance Imaging. *Chem Commun* **2010**, *46* (1), 73–75. https://doi.org/10.1039/B916562B.

(10) Hugounenq, P.; Levy, M.; Alloyeau, D.; Lartigue, L.; Dubois, E.; Cabuil, V.; Ricolleau, C.; Roux, S.; Wilhelm, C.; Gazeau, F.; Bazzi, R. Iron Oxide Monocrystalline Nanoflowers for Highly Efficient Magnetic Hyperthermia. *J. Phys. Chem. C* **2012**, *116* (29), 15702–15712. https://doi.org/10.1021/jp3025478.

(11) Espinosa, A.; Kolosnjaj-Tabi, J.; Abou-Hassan, A.; Plan Sangnier, A.; Curcio, A.; Silva, A. K. A.; Di Corato, R.; Neveu, S.; Pellegrino, T.; Liz-Marzán, L. M.; Wilhelm, C. Magnetic (Hyper)Thermia or Photothermia? Progressive Comparison of Iron Oxide and Gold Nanoparticles Heating in Water, in Cells, and *in Vivo*. *Adv. Funct. Mater.* **2018**, *28* (37), 1803660. https://doi.org/10.1002/adfm.201803660.

(12) Lartigue, L.; Hugounenq, P.; Alloyeau, D.; Clarke, S. P.; Lévy, M.; Bacri, J.-C.; Bazzi, R.; Brougham, D. F.; Wilhelm, C.; Gazeau, F. Cooperative Organization in Iron Oxide Multi-Core Nanoparticles Potentiates Their Efficiency as Heating Mediators and MRI Contrast Agents. *ACS Nano* **2012**, *6* (12), 10935–10949. https://doi.org/10.1021/nn304477s.

(13) Dutta, P.; Pal, S.; Seehra, M. S.; Shah, N.; Huffman, G. P. Size Dependence of Magnetic Parameters and Surface Disorder in Magnetite Nanoparticles. *J. Appl. Phys.* **2009**, *105* (7), 07B501. https://doi.org/10.1063/1.3055272.

(14) Shaw, S. K.; Kailashiya, J.; Gangwar, A.; Alla, S. K.; Gupta, S. K.; Prajapat, C. L.; Meena, S. S.; Dash, D.; Maiti, P.; Prasad, N. K. γ-Fe2O3 Nanoflowers as Efficient Magnetic Hyperthermia and Photothermal Agent. *Appl. Surf. Sci.* **2021**, *560*, 150025. https://doi.org/10.1016/j.apsusc.2021.150025.

(15) Cabana, S.; Curcio, A.; Michel, A.; Wilhelm, C.; Abou-Hassan, A. Iron Oxide Mediated Photothermal Therapy in the Second Biological Window: A Comparative Study between Magnetite/Maghemite Nanospheres and Nanoflowers. *Nanomaterials* **2020**, *10* (8), 1548. https://doi.org/10.3390/nano10081548.

(16) Frison, R.; Cernuto, G.; Cervellino, A.; Zaharko, O.; Colonna, G. M.; Guagliardi, A.; Masciocchi, N. Magnetite–Maghemite Nanoparticles in the 5–15 Nm Range: Correlating the Core–Shell Composition and the Surface Structure to the Magnetic Properties. A Total Scattering Study. *Chem. Mater.* **2013**, *25* (23), 4820–4827. https://doi.org/10.1021/cm403360f.

(17) Bender, P.; Fock, J.; Frandsen, C.; Hansen, M. F.; Balceris, C.; Ludwig, F.; Posth, O.; Wetterskog, E.; Bogart, L. K.; Southern, P.; Szczerba, W.; Zeng, L.; Witte, K.; Grüttner, C.; Westphal, F.; Honecker, D.; González-Alonso, D.; Fernández Barquín, L.; Johansson, C. Relating Magnetic Properties and High Hyperthermia Performance of Iron Oxide Nanoflowers. *J. Phys. Chem. C* **2018**, *122* (5), 3068–3077. https://doi.org/10.1021/acs.jpcc.7b11255.

(18) Kolhatkar, A.; Jamison, A.; Litvinov, D.; Willson, R.; Lee, T. Tuning the Magnetic Properties of Nanoparticles. *Int. J. Mol. Sci.* **2013**, *14* (8), 15977–16009.

https://doi.org/10.3390/ijms140815977.
(19) Espinosa, D.; Carlsson, L. B.; Neto, A. M. F.; Alves, S. Influence of Nanoparticle Size on the Nonlinear Optical Properties of Magnetite Ferrofluids. *Phys. Rev. E* **2013**, *88* (3), 032302. https://doi.org/10.1103/PhysRevE.88.032302.
(20) Gavilán, H.; Sánchez, E. H.; Brollo, M. E. F.; Asín, L.; Moerner, K. K.; Frandsen, C.; Lázaro, F. J.; Serna, C. J.; Veintemillas-Verdaguer, S.; Morales, M. P.; Gutiérrez, L. Formation Mechanism of Maghemite Nanoflowers Synthesized by a Polyol-Mediated Process. *ACS Omega* **2017**, *2* (10), 7172–7184. https://doi.org/10.1021/acsomega.7b00975.
(21) Gauvin Hemery; Anthony C Keyes. Tuning Sizes, Morphologies, and Magnetic Properties of Monocore *Versus* Multicore Iron Oxide Nanoparticles through the Controlled Addition of Water in the Polyol Synthesis. *Inorg Chem* **2017**, 12.
(22) Freis, B.; Cotin, G.; Perton, F.; Mertz, D.; Boutry, S.; Laurent, S.; Begin-Colin, S. The Size, Shape, and Composition Design of Iron Oxide Nanoparticles to Combine, MRI, Magnetic Hyperthermia, and Photothermia. In *Magnetic Nanoparticles in Human Health and Medicine*; Caizer, C., Rai, M., Eds.; Wiley, 2021; pp 380–429. https://doi.org/10.1002/9781119754725.ch17.
(23) Zhang, L.; Dou, Y.-H.; Gu, H.-C. Sterically Induced Shape Control of Magnetite Nanoparticles. *J. Cryst. Growth* **2006**, *296* (2), 221–226. https://doi.org/10.1016/j.jcrysgro.2006.08.010.
(24) Nikitin, A. A.; Shchetinin, I. V.; Tabachkova, N. Yu.; Soldatov, M. A.; Soldatov, A. V.; Sviridenkova, N. V.; Beloglazkina, E. K.; Savchenko, A. G.; Fedorova, N. D.; Abakumov, M. A.; Majouga, A. G. Synthesis of Iron Oxide Nanoclusters by Thermal Decomposition. *Langmuir* **2018**, *34* (15), 4640–4650. https://doi.org/10.1021/acs.langmuir.8b00753.
(25) Fievet, F.; Lagier, J. P.; Figlarz, M. Monodisperse Métal Powders in Micrometer and Submicrometer Sizes by the Polyol Process. *MRS Bull.* 6.
(26) Fiévet, F.; Ammar-Merah, S.; Brayner, R.; Chau, F.; Giraud, M.; Mammeri, F.; Peron, J.; Piquemal, J.-Y.; Sicard, L.; Viau, G. The Polyol Process: A Unique Method for Easy Access to Metal Nanoparticles with Tailored Sizes, Shapes and Compositions. *Chem. Soc. Rev.* **2018**, *47* (14), 5187–5233. https://doi.org/10.1039/C7CS00777A.
(27) Maity, D.; Chandrasekharan, P.; Si-Shen, F.; Xue, J.-M.; Ding, J. Polyol-Based Synthesis of Hydrophilic Magnetite Nanoparticles. *J. Appl. Phys.* **2010**, *107* (9), 09B310. https://doi.org/10.1063/1.3355898.
(28) Abbas, M.; Parvatheeswara Rao, B.; Abdel-Hamed, M. O.; Kim, C. Modified Polyol Route for Synthesis of Fe3O4/Ag and α-Fe/Ag Nanocomposite. *J. Alloys Compd.* **2014**, *615*, S308–S312. https://doi.org/10.1016/j.jallcom.2014.01.224.
(29) Caruntu, D.; Caruntu, G.; Chen, Y.; O'Connor, C. J.; Goloverda, G.; Kolesnichenko, V. L. Synthesis of Variable-Sized Nanocrystals of Fe3O4 with High Surface Reactivity. 8.
(30) Caruntu, D.; Remond, Y.; Chou, N. H.; Jun, M.-J.; Caruntu, G.; He, J.; Goloverda, G.; O'Connor, C.; Kolesnichenko, V. Reactivity of 3d Transition Metal Cations in Diethylene Glycol Solutions. Synthesis of Transition Metal Ferrites with the Structure of Discrete Nanoparticles Complexed with Long-Chain Carboxylate Anions. *Inorg. Chem.* **2002**, *41* (23), 6137–6146. https://doi.org/10.1021/ic025664j.
(31) Cheng, C.; Xu, F.; Gu, H. Facile Synthesis and Morphology Evolution of Magnetic Iron Oxide Nanoparticles in Different Polyol Processes. *New J. Chem.* **2011**, *35* (5), 1072. https://doi.org/10.1039/c0nj00986e.
(32) Roca, A. G.; Gutiérrez, L.; Gavilán, H.; Fortes Brollo, M. E.; Veintemillas-Verdaguer, S.; Morales, M. del P. Design Strategies for Shape-Controlled Magnetic Iron Oxide Nanoparticles. *Adv. Drug Deliv. Rev.* **2019**, *138*, 68–104. https://doi.org/10.1016/j.addr.2018.12.008.
(33) Wetegrove, M.; Witte, K.; Bodnar, W.; Pfahl, D.-E.; Springer, A.; Schell, N.;

Westphal, F.; Burkel, E. Formation of Maghemite Nanostructures in Polyol: Tuning the Particle Size *via* the Precursor Stoichiometry. *CrystEngComm* **2019**, *21* (12), 1956–1966. https://doi.org/10.1039/C8CE02115E.
(34) Gallo-Cordova, A.; Ovejero, J. G.; Pablo-Sainz-Ezquerra, A. M.; Cuya, J.; Jeyadevan, B.; Veintemillas-Verdaguer, S.; Tartaj, P.; Morales, M. del P. Unravelling an Amine-Regulated Crystallization Crossover to Prove Single/Multicore Effects on the Biomedical and Environmental Catalytic Activity of Magnetic Iron Oxide Colloids. *J. Colloid Interface Sci.* **2022**, *608*, 1585–1597. https://doi.org/10.1016/j.jcis.2021.10.111.
(35) Mirabello, G.; Keizer, A.; Bomans, P. H. H.; Kovács, A.; Dunin-Borkowski, R. E.; Sommerdijk, N. A. J. M.; Friedrich, H. Understanding the Formation Mechanism of Magnetic Mesocrystals with (Cryo-)Electron Microscopy. *Chem. Mater.* **2019**, *31* (18), 7320–7328. https://doi.org/10.1021/acs.chemmater.9b01836.
(36) Cotin, G.; Blanco-Andujar, C.; Perton, F.; Asín, L.; de la Fuente, J. M.; Reichardt, W.; Schaffner, D.; Ngyen, D.-V.; Mertz, D.; Kiefer, C.; Meyer, F.; Spassov, S.; Ersen, O.; Chatzidakis, M.; Botton, G. A.; Hénoumont, C.; Laurent, S.; Greneche, J.-M.; Teran, F. J.; Ortega, D.; *et al.* Unveiling the Role of Surface, Size, Shape and Defects of Iron Oxide Nanoparticles for Theranostic Applications. *Nanoscale* **2021**, *13* (34), 14552–14571. https://doi.org/10.1039/D1NR03335B.
(37) Talbot, D.; Abramson, S.; Griffete, N.; Bée, A. PH-Sensitive Magnetic Alginate/γ-Fe2O3 Nanoparticles for Adsorption/Desorption of a Cationic Dye from Water. *J. Water Process Eng.* **2018**, *25*, 301–308. https://doi.org/10.1016/j.jwpe.2018.08.013.
(38) Annersten, H.; Hafner, S. S. Vacancy Distribution in Synthetic Spinels of the Series Fe304—y-Fe203. 20.
(39) Gorski, C. A.; Scherer, M. M. Determination of Nanoparticulate Magnetite Stoichiometry by Mossbauer Spectroscopy, Acidic Dissolution, and Powder X-Ray Diffraction: A Critical Review. *Am. Mineral.* **2010**, *95* (7), 1017–1026. https://doi.org/10.2138/am.2010.3435.
(40) Gotić, M.; Koščec, G.; Musić, S. Study of the Reduction and Reoxidation of Substoichiometric Magnetite. *J. Mol. Struct.* **2009**, *924–926*, 347–354. https://doi.org/10.1016/j.molstruc.2008.10.048.
(41) Schmidbauer, E.; Keller, M. Magnetic Hysteresis Properties, Mössbauer Spectra and Structural Data of Spherical 250nm Particles of Solid Solutions —. *J. Magn. Magn. Mater.* **2006**, *297* (2), 107–117. https://doi.org/10.1016/j.jmmm.2005.02.063.
(42) Voleník, K.; Seberíni, M.; Neid, J. A Mössbauer and X-Ray Diffraction Study of Nonstoichiometry in Magnetite. *Czechoslov. J. Phys.* **1975**, *25* (9), 1063–1071. https://doi.org/10.1007/BF01597585.
(43) Yang, J. B.; Zhou, X. D.; Yelon, W. B.; James, W. J.; Cai, Q.; Gopalakrishnan, K. V.; Malik, S. K.; Sun, X. C.; Nikles, D. E. Magnetic and Structural Studies of the Verwey Transition in Fe3−δO4 Nanoparticles. *J. Appl. Phys.* **2004**, *95* (11), 7540–7542. https://doi.org/10.1063/1.1669344.
(44) Sun, Z.; Yan, W.; Yao, T.; Liu, Q.; Xie, Y.; Wei, S. XAFS in Dilute Magnetic Semiconductors. *Dalton Trans.* **2013**, *42* (38), 13779. https://doi.org/10.1039/c3dt50888a.
(45) Kuzmin, A.; Chaboy, J. EXAFS and XANES Analysis of Oxides at the Nanoscale. *IUCrJ* **2014**, *1* (6), 571–589. https://doi.org/10.1107/S2052252514021101.
(46) Fdez-Gubieda, M. L.; García-Prieto, A.; Alonso, J.; Meneghini, C. X-Ray Absorption Fine Structure Spectroscopy in Fe Oxides and Oxyhydroxides. In *Iron Oxides*; Faivre, D., Ed.; Wiley, 2016; pp 397–422. https://doi.org/10.1002/9783527691395.ch17.
(47) Šutka, A.; Lagzdina, S.; Käämbre, T.; Pärna, R.; Kisand, V.; Kleperis, J.; Maiorov, M.; Kikas, A.; Kuusik, I.; Jakovlevs, D. Study of the Structural Phase Transformation of Iron Oxide Nanoparticles from an Fe2+ Ion Source by Precipitation under Various Synthesis

Parameters and Temperatures. *Mater. Chem. Phys.* **2015**, *149–150*, 473–479. https://doi.org/10.1016/j.matchemphys.2014.10.048.

(48) Wilke, M.; Farges, F.; Petit, P.-E.; Brown, G. E.; Martin, F. Oxidation State and Coordination of Fe in Minerals: An Fe *K*- XANES Spectroscopic Study. *Am. Mineral.* **2001**, *86* (5–6), 714–730. https://doi.org/10.2138/am-2001-5-612.

(49) Petit, P.-E.; Farges, F.; Wilke, M.; Solé, V. A. Determination of the Iron Oxidation State in Earth Materials Using XANES Pre-Edge Information. *J. Synchrotron Radiat.* **2001**, *8* (2), 952–954. https://doi.org/10.1107/S0909049500021063.

(50) Piquer, C.; Laguna-Marco, M. A.; Roca, A. G.; Boada, R.; Guglieri, C.; Chaboy, J. Fe K-Edge X-Ray Absorption Spectroscopy Study of Nanosized Nominal Magnetite. *J. Phys. Chem. C* **2014**, *118* (2), 1332–1346. https://doi.org/10.1021/jp4104992.

(51) Rubio-Zuazo, J.; Chainani, A.; Taguchi, M.; Malterre, D.; Serrano, A.; Castro, G. R. Electronic Structure of FeO, γ − Fe 2 O 3 , and Fe 3 O 4 Epitaxial Films Using High-Energy Spectroscopies. *Phys. Rev. B* **2018**, *97* (23), 235148. https://doi.org/10.1103/PhysRevB.97.235148.

(52) Gerber, O.; Pichon, B. P.; Ulhaq, C.; Grenèche, J.-M.; Lefevre, C.; Florea, I.; Ersen, O.; Begin, D.; Lemonnier, S.; Barraud, E.; Begin-Colin, S. Low Oxidation State and Enhanced Magnetic Properties Induced by Raspberry Shaped Nanostructures of Iron Oxide. *J. Phys. Chem. C* **2015**, *119* (43), 24665–24673. https://doi.org/10.1021/acs.jpcc.5b08164.

(53) Gerber, O.; Pichon, B. P.; Ihiawakrim, D.; Florea, I.; Moldovan, S.; Ersen, O.; Begin, D.; Grenèche, J.-M.; Lemonnier, S.; Barraud, E.; Begin-Colin, S. Synthesis Engineering of Iron Oxide Raspberry-Shaped Nanostructures. *Nanoscale* **2017**, *9* (1), 305–313. https://doi.org/10.1039/C6NR07567C.

(54) Doriguetto, A. C.; Fernandes, N. G.; Persiano, A. I. C.; Filho, E. N.; Grenèche, J. M.; Fabris, J. D. Characterization of a Natural Magnetite. *Phys. Chem. Miner.* **2003**, *30* (5), 249–255. https://doi.org/10.1007/s00269-003-0310-x.

(55) Sharifi Dehsari, H.; Ksenofontov, V.; Möller, A.; Jakob, G.; Asadi, K. Determining Magnetite/Maghemite Composition and Core–Shell Nanostructure from Magnetization Curve for Iron Oxide Nanoparticles. *J. Phys. Chem. C* **2018**, *122* (49), 28292–28301. https://doi.org/10.1021/acs.jpcc.8b06927.

(56) Santoyo Salazar, J.; Perez, L.; de Abril, O.; Truong Phuoc, L.; Ihiawakrim, D.; Vazquez, M.; Greneche, J.-M.; Begin-Colin, S.; Pourroy, G. Magnetic Iron Oxide Nanoparticles in 10−40 Nm Range: Composition in Terms of Magnetite/Maghemite Ratio and Effect on the Magnetic Properties. *Chem. Mater.* **2011**, *23* (6), 1379–1386. https://doi.org/10.1021/cm103188a.

(57) Goya, G. F.; Berquó, T. S.; Fonseca, F. C.; Morales, M. P. Static and Dynamic Magnetic Properties of Spherical Magnetite Nanoparticles. *J. Appl. Phys.* **2003**, *94* (5), 3520–3528. https://doi.org/10.1063/1.1599959.

(58) Chen, D.-X.; Sanchez, A.; Taboada, E.; Roig, A.; Sun, N.; Gu, H.-C. Size Determination of Superparamagnetic Nanoparticles from Magnetization Curve. *J. Appl. Phys.* **2009**, *105* (8), 083924. https://doi.org/10.1063/1.3117512.

(59) Jordan, A.; Scholz, R.; Wust, P.; Fa, H. Magnetic #uid Hyperthermia (MFH): Cancer Treatment with AC Magnetic "eld Induced Excitation of Biocompatible Superparamagnetic Nanoparticles. *J. Magn. Magn. Mater.* **1999**, 7.

(60) Kostopoulou, A.; Lappas, A. Colloidal Magnetic Nanocrystal Clusters: Variable Length-Scale Interaction Mechanisms, Synergetic Functionalities and Technological Advantages. *Nanotechnol. Rev.* **2015**, *4* (6). https://doi.org/10.1515/ntrev-2014-0034.

(61) Tang, J.; Myers, M.; Bosnick, K. A.; Brus, L. E. Magnetite Fe $_3$ O $_4$ Nanocrystals: Spectroscopic Observation of Aqueous Oxidation Kinetics †. *J. Phys. Chem. B* **2003**, *107* (30), 7501–7506. https://doi.org/10.1021/jp027048e.

(62) Link, S.; Mohamed, M. B.; El-Sayed, M. A. Simulation of the Optical Absorption Spectra of Gold Nanorods as a Function of Their Aspect Ratio and the Effect of the Medium Dielectric Constant. *J. Phys. Chem. B* **1999**, *103* (16), 3073–3077. https://doi.org/10.1021/jp990183f.

(63) Fontijn, W. F. J.; van der Zaag, P. J.; Devillers, M. A. C.; Brabers, V. A. M.; Metselaar, R. Optical and Magneto-Optical Polar Kerr Spectra of Fe 3 O 4 and Mg 2 + - or Al 3 + -Substituted Fe 3 O 4. *Phys. Rev. B* **1997**, *56* (9), 5432–5442. https://doi.org/10.1103/PhysRevB.56.5432.

(64) https://github.com/scottprahl/miepython

(65) Cooper, S. R.; Plummer, L. K.; Cosby, A. G.; Lenox, P.; Jander, A.; Dhagat, P.; Hutchison, J. E. Insights into the Magnetic Properties of Sub-10 Nm Iron Oxide Nanocrystals through the Use of a Continuous Growth Synthesis. *Chem. Mater.* **2018**, *30* (17), 6053–6062. https://doi.org/10.1021/acs.chemmater.8b02389.

(66) Ge, X.; Fu, Q.; Bai, L.; Chen, B.; Wang, R.; Gao, S.; Song, J. Photoacoustic Imaging and Photothermal Therapy in the Second Near-Infrared Window. *New J. Chem.* **2019**, *43* (23), 8835–8851. https://doi.org/10.1039/C9NJ01402K.

(67) Belin, T.; Guigue-Millot, N.; Caillot, T.; Aymes, D.; Niepce, J. C. Influence of Grain Size, Oxygen Stoichiometry, and Synthesis Conditions on the γ-Fe2O3 Vacancies Ordering and Lattice Parameters. *J. Solid State Chem.* **2002**, *163* (2), 459–465. https://doi.org/10.1006/jssc.2001.9426.

(68) Sadat, M. E.; Kaveh Baghbador, M.; Dunn, A. W.; Wagner, H. P.; Ewing, R. C.; Zhang, J.; Xu, H.; Pauletti, G. M.; Mast, D. B.; Shi, D. Photoluminescence and Photothermal Effect of Fe_3O_4 Nanoparticles for Medical Imaging and Therapy. *Appl. Phys. Lett.* **2014**, *105* (9), 091903. https://doi.org/10.1063/1.4895133.

(69) Akshay, V. R.; Arun, B.; Mandal, G.; Vasundhara, M. Visible Range Optical Absorption, Urbach Energy Estimation and Paramagnetic Response in Cr-Doped TiO_2 Nanocrystals Derived by a Sol–Gel Method. *Phys. Chem. Chem. Phys.* **2019**, *21* (24), 12991–13004. https://doi.org/10.1039/C9CP01351B.

(70) Hassanien, A. S.; Akl, A. A. Effect of Se Addition on Optical and Electrical Properties of Chalcogenide CdSSe Thin Films. *Superlattices Microstruct.* **2016**, *89*, 153–169. https://doi.org/10.1016/j.spmi.2015.10.044.

(71) Wasim, S. M.; Rincón, C.; Marín, G.; Bocaranda, P.; Hernández, E.; Bonalde, I.; Medina, E. Effect of Structural Disorder on the Urbach Energy in Cu Ternaries. *Phys. Rev. B* **2001**, *64* (19), 195101. https://doi.org/10.1103/PhysRevB.64.195101.

(72) Ghandoor, H. E.; Zidan, H. M.; Khalil, M. M. H.; Ismail, M. I. M. Synthesis and Some Physical Properties of Magnetite (Fe3O4) Nanoparticles. *Int J Electrochem Sci* **2012**, *7*, 12.

(73) Absorption Edge, Urbach Rule, Exciton (Electron)-Phonon Interaction, Disordering. *Int. J. Opt. Appl.* **2014**, 8.

(74) Plan Sangnier, A.; Preveral, S.; Curcio, A.; K. A. Silva, A.; Lefèvre, C. T.; Pignol, D.; Lalatonne, Y.; Wilhelm, C. Targeted Thermal Therapy with Genetically Engineered Magnetite Magnetosomes@RGD: Photothermia Is Far More Efficient Than Magnetic Hyperthermia. *J. Controlled Release* **2018**, *279*, 271–281. https://doi.org/10.1016/j.jconrel.2018.04.036.

(75) Maibam, B.; Baruah, S.; Kumar, S. Photoluminescence and Intrinsic Ferromagnetism of Fe Doped Zinc Oxide. *SN Appl. Sci.* **2020**, *2* (10), 1712. https://doi.org/10.1007/s42452-020-03519-y.

(76) Pathak, N.; Ghosh, P. S.; Gupta, S. K.; Mukherjee, S.; Kadam, R. M.; Arya, A. An Insight into the Various Defects-Induced Emission in $MgAl_2O_4$ and Their Tunability with Phase Behavior: Combined Experimental and Theoretical Approach. *J. Phys. Chem. C* **2016**, *120* (7), 4016–4031. https://doi.org/10.1021/acs.jpcc.5b11822.

(77) Judith Vijaya, J.; Sekaran, G.; Bououdina, M. Effect of Cu2+ Doping on Structural, Morphological, Optical and Magnetic Properties of MnFe2O4 Particles/Sheets/Flakes-Like Nanostructures. *Ceram. Int.* **2015**, *41* (1), 15–26. https://doi.org/10.1016/j.ceramint.2013.10.145.

(78) Choudhury, B.; Choudhury, A. Oxygen Defect Dependent Variation of Band Gap, Urbach Energy and Luminescence Property of Anatase, Anatase–Rutile Mixed Phase and of Rutile Phases of TiO2 Nanoparticles. *Phys. E Low-Dimens. Syst. Nanostructures* **2014**, *56*, 364–371. https://doi.org/10.1016/j.physe.2013.10.014.

(79) Ghamnia, M.; Jardin, C.; Bouslama, M. Luminescent Centres F and F+ in α-Alumina Detected by Cathodoluminescence Technique. *J. Electron Spectrosc. Relat. Phenom.* **2003**, *133* (1–3), 55–63. https://doi.org/10.1016/j.elspec.2003.08.003.

(80) Müller, M.; Jüstel, T. Energy Transfer and Unusual Decay Behaviour of $BaCa_2Si_3O_9$:Eu^{2+},Mn^{2+} Phosphor. *Dalton Trans.* **2015**, *44* (22), 10368–10376. https://doi.org/10.1039/C5DT00591D.

(81) Wang, Z.; Wang, L. Role of Oxygen Vacancy in Metal Oxide Based Photoelectrochemical Water Splitting. *EcoMat* **2021**, *3* (1). https://doi.org/10.1002/eom2.12075.

(82) Liao, P.; Toroker, M. C.; Carter, E. A. Electron Transport in Pure and Doped Hematite. *Nano Lett.* **2011**, *11* (4), 1775–1781. https://doi.org/10.1021/nl200356n.